Oral presentation | Turbulence simulation (DNS,LES,RANS)

Turbulence simulation(DNS,LES,RANS)-I

Wed. Jul 17, 2024 2:00 PM - 4:00 PM Room B

[8-B-03] Roughness induced instability and subcritical bypass transition in the high-speed leading-edge boundary layer

*Youcheng Xi[1], Song Fu[1] (1. Tsinghua University)

Keywords: subcritical transition, roughness induced, leading-edge boundary layer

©Retained by Authors

Twelfth International Conference on
Computational Fluid Dynamics (ICCFD12),
Kobe, Japan, July 14-19, 2024

Roughness induced instability and subcritical bypass transition in the high-speed leading-edge boundary layer

Youcheng, Xi* and Song. Fu*
Corresponding author: xiyc@mail.tsinghua.edu.cn
* School of Aerospace Engineering, Tsinghua Universitym 100084, Beijing, China.

Abstract: The attachment-line boundary layer is critical in hypersonic flows due to its significant impact on heat transfer and aerodynamic performance. In this study, high-fidelity numerical simulations are conducted to uncover the complete processes of subcritical roughness-induced laminar-turbulent transition at the leading-edge attachment-line boundary layer of a blunt swept body under hypersonic experimental conditions. Two roughness elements of different heights are examined. For the lower-height roughness element, additional unsteady perturbations are required to trigger a transition in the wake, suggesting that the flow field behind the roughness element acts as a disturbance amplifier for upstream perturbations. Conversely, a higher roughness element can independently induce the transition. A low-frequency absolute instability is detected behind the roughness, leading to the formation of streaks. The secondary instabilities of these streaks are identified as the direct cause of the final transition. Finally, the characteristis of the resulting three-dimensional turbulent boundary layer are discussed. It is found that some advanced law-of-the-walls, proposed based on statstical two dimensional boundary layer, are also applicable to three-dimensional boundary layers under conditions involving crossflow and pressure gradients. The analysis of Reynolds stress and turbulent kinetic energy budgets indicates that the fundamental features of the three-dimensional turbulent boundary layer are consistent with those of two-dimensional cases.

Keywords: attachment line boundary layer, roughness-induced subcritical transition, three-dimensional turbulent boundary layer,

1 Introduction

The subcritical transition of leading-edge boundary layer near the attachment line of swept wings plays an important role in aerodynamic, which means the boundary layer may undergo transition to turbulence below the critical Reynolds number predicted by linear stability theory(LST). This phonomenon is especially critical because turbulent flow that starts at the leading edge of a swept wing can propagate downstream, affecting extensive regions of the wing's chord and compromising its overall aerodynamic performance.

As the actual flow is three-dimensional in nature, to simplify the problem, it is common to employ the swept Hiemenz boundary layer past a flat plate[1, 2] as an approximation model for the actual three-dimensional boundary layer[3, 4, 5, 6] around the leading edge. Based on this model, the LST performed by [4] gives a linear critical Reynolds number of $Re_{crit} \approx 583.1$, which is in good agreement with the previous experimental finding [3] as well as the numerical simulation by Spalart [7]. However, in many experimental tests[8, 3, 9], transitions are often observed at a significantly lower value $Re_{tr} \approx 250$, if the boundary layer is subject to sufficiently large external disturbulences. In order to understand the discrepancy between linear stability results and experimental findings, finite amplitude perturbations and nonlinear processes have to be taken into account. The group of Prof. Kleiser[10, 11, 12] carried out direct numerical simulations on a swept Hiemenz boundary layer with a pair of stationary counter-rotating streamwise vortex-like structures with finite amplitude. A bypass transition scenario has been identified, which can explain the occurrence of subcritical transition in experiments. The initial pair of stationary counter-rotating vortex-like structures lead to the transient growth of streaks according to the lift-up effect, and then the damped primary vortices and streaks interacts with unsteady secondary perturbations, causing secondary instabilities and leading to the final transition to turbulence.

However, the aforementioned conclusions are based on incompressible flow only. When compressible effects (such as Mach number, shock waves, wall temperature, etc.) are taken into account, the problem becomes significantly more complex. Based on previous studies[13, 14, 15, 16, 17, 18], for large sweep Mach numbers, the attachment-line mode is inviscid in nature, while for lower sweep Mach numbers, the attachment-line instability exhibits the behaviours of viscous Tollmien–Schlichting waves. Detailed reviews for these research have been included in our previous studies[16, 17] and the connection between the linear stability features of the flow and the issues discussed in this study is not particularly direct. Therefore, we will not elaborate on them here.

In fact, experimental investigations of high-speed attachment-line flow date back to 1959. Initially, [19] focused on the effects of sweep angles and heat flux along the attachment line in supersonic conditions. They detected the transition of attachment-line flow in their Mach 4.15 experiments, studying the effect of sweep angles over a relatively wide range. Later, [20, 21] conducted experiments with a free-stream Mach number of 3.5 and various sweep angles, also detecting transition along the attachment line and finding transition Reynolds numbers around 650 (based on the boundary layer length scale at the leading edge). [22] performed similar tests to validate Creel et al.'s results. [23] studied hypersonic attachment-line flow in a Ludwieg-tube wind tunnel. In some conditions, the bypass scenario is the most possible reasons for the transition. During the experiments, without the end plates and trip wires, the attachment-line boundary layer can keep laminar along the entire attachment line.

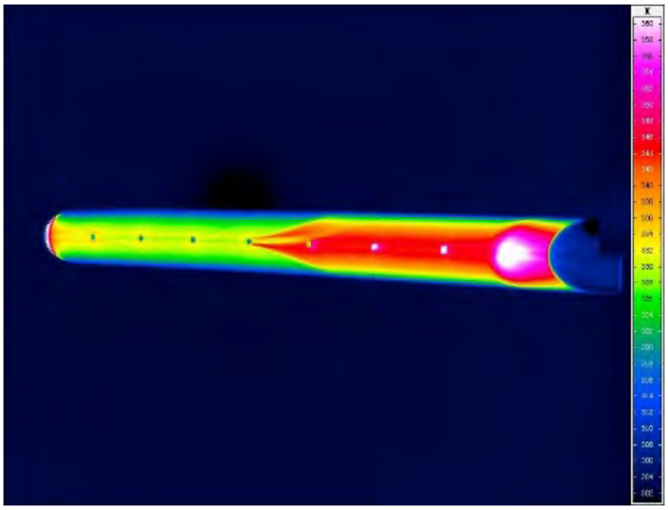

Figure 1: Infrared measurements of the temperature distribution along the leading edge of the swept blunt body. Dots indicate the positions of the pressure sensors; pink represents high-temperature regions, while blue indicates low-temperature regions.

Recently, experimental tests are performed over a swept blunt leading edge, with a swept angle of 45^o, in the FD-07 Mach 6.0 hypersonic wind tunnel of the China Academy of Aerospace Aerodynamics. During the experiment, despite high levels of external perturbations, the attachment-line boundary layer remained laminar. When pressure sensors are mounted at the attachment-line position on the leading edge of a swept blunt body model, the surface of the model is no longer smooth. Due to unavoidable installation errors during the experiment, effective roughness elements, such as small protrusions or depressions, form along the attachment line. Experiments with this configuration have shown that disturbances induced by these roughness elements can effectively trigger the transition of the attachment-line boundary layer to turbulence, as shown in figure 1.

Previous studies indicate that the phenomenon of subcritical transition is highly significant in the context of attachment-line flows. However, most of these studies have been limited to incompressible flows or confined to linear analysis, leaving a significant gap in the understanding of subcritical compressible flows. Furthermore, even in incompressible flow scenarios, existing computational analyses have often employed simplified models or introduced artificial disturbances to facilitate numerical studies, raising questions about their validity under actual conditions. Therefore, it is imperative to conduct numerical investigations of the three-dimensional boundary layer at the leading edge of compressible blunt bodies under relative realistic conditions. In this study, we perform numerical simulations of transitional high-speed attachment-line boundary layers that develop from finite amplitude initial disturbances. These simulations correspond to experimental investigations of roughness-induced transition over a real blunt configuration, without assuming an infinite span. Unlike typical transitional studies, we have calculated the complete transition to turbulence over a real configuration. Our primary aim is to investigate the physical mechanisms of transition induced by roughness elements in three-dimensional attachment-line boundary layers at the leading edge. Additionally, we focus on the characteristics of turbulence, particularly the variations in mean flow properties and fundamental statistical quantities.

This paper is organized as follows. In section 2, the governing equations are introduced as well as the details for numerical simulations. The results for transitional and turbulent three-dimensional boundary layers are presented in section 3 and the conclusions and some discussions are given in section 4.

2 Methodology

2.1 Governing equations

The governing equations for all simulations in this work are the dimensionless compressible Navier–Stokes(NS) equations for a Newtonian fluid, which can be written as:

$$\frac{\partial Q}{\partial t} + \frac{\partial F_j}{\partial x_j} + \frac{\partial F_j^v}{\partial x_j} = 0, \tag{1}$$

$$Q = \left[\rho, \rho u_1, \rho u_2, \rho u_3, E_t\right]^T, \tag{2}$$

$$F_j = \begin{bmatrix} \rho u_j \\ \rho u_1 u_j + p\delta_{1j} \\ \rho u_2 u_j + p\delta_{2j} \\ \rho u_3 u_j + p\delta_{3j} \\ (E_t + p)\, u_j \end{bmatrix}, F_j^v = \begin{bmatrix} 0 \\ \tau_{1j} \\ \tau_{2j} \\ \tau_{3j} \\ \tau_{jk} u_k - q_j \end{bmatrix}. \tag{3}$$

Throughout this work the coordinates $x_i, (i = 1, 2, 3)$ are referred to as x, y, z, respectively, with corresponding velocity components $u_1 = u, u_2 = v, u_3 = w$. F_j and F_j^v stand for the inviscid and viscous flux. The total energy E_t and the viscous stress τ_{ij} are given as, respectively,

$$\begin{aligned} E_t &= \rho\left(\frac{T}{\gamma(\gamma-1)M_\infty^2} + \frac{u_k u_k}{2}\right), \\ \tau_{ij} &= \frac{\mu}{Re_\infty}\left(\frac{\partial u_i}{\partial x_j} + \frac{\partial u_j}{\partial x_i} - \frac{2}{3}\delta_{ij}\frac{\partial u_k}{\partial x_k}\right). \end{aligned} \tag{4}$$

The pressure p and heat flux q_i are obtained from:

$$p = \frac{\rho T}{\gamma M_\infty^2}, \quad q_i = -\frac{\mu}{(\gamma-1)M_\infty^2 Re_\infty Pr}\frac{\partial T}{\partial x_i}. \tag{5}$$

The viscosity is calculated using the Sutherland law

$$\mu = T^{3/2}\frac{T_\infty + C}{T \cdot T_\infty + C}, \tag{6}$$

with $C = 110.4K$. The free-stream Reynolds number Re_∞, Mach number M_∞ and Prandtl number Pr are defined as

$$Re_\infty = \frac{\rho_\infty^* U_\infty^* l_0^*}{\mu_\infty^*}, \quad M_\infty = \frac{U_\infty^*}{\sqrt{\gamma R_g^* T_\infty^*}}, \quad Pr = 0.72, \tag{7}$$

where ρ_∞^*, U_∞^*, T_∞^* and μ_∞^* stand for the freestream density, velocity, temperature and viscosity, respectively. $R_g^* = 287\mathrm{J}/(\mathrm{K}\cdot\mathrm{Kg})$ represents the gas constant and γ stands for the ratio of specific heat. The length scale l_0^* is chosen as 1 millimeter in this research. The $*$ denotes dimensional flow parameters.

2.2 Numerical method

Two solvers have been employed in this study. The first code we use to perform computations is the high-order finite difference code developed recently at Tsinghua University. A shock-fitting (S-F) method [24] is used to compute steady hypersonic viscous flow together with the high-order accurate non-compact centre finite differences methods. The fifth-order upwind scheme (for inviscid flux F_j) and the 6th-order centre scheme (for viscous flux F_{vj}) are used to compute the flow field. A 4th-order Runge-Kutta method is applied for the time integration, and the simulations are performed until the maximum residual reaches a small value on the order of 10^{-15}. A full implicit scheme can also be used for fast convergence. Validations of the code and some applications for calorically perfect gas and thermal-chemical non-equilibrium flow can be found in our previous study[16, 17, 25]. The solver is used mainly to determing the location of the leading shock and give a high quality initial field.

The second code, used in this study, is a well-validated fluid dynamic shock capture (S-C) solver OPENCFD, developed by Li et al[26], which is mainly used to simulate the whole transition/turbulent processes. The code has been validated and verified in previous studies[26, 27, 28]. For three-dimensional calculations presented in this study, a hybrid high-order finite difference scheme, including the seventh-order upwind scheme, fifth-order and seventh-order WENO schemes[29], together with a shock sensor[30] is used for the inviscid flux in the characteristic form. Based on that formular, during the calculation, more than 98% of the regions use the linear seventh-order upwind scheme, only a few regions corresponding to discontinuities use the nonlinear WENO schemes, which greatly increase the calculation efficiency. A standard sixth-order central difference scheme is used for viscous flux.

2.3 Models

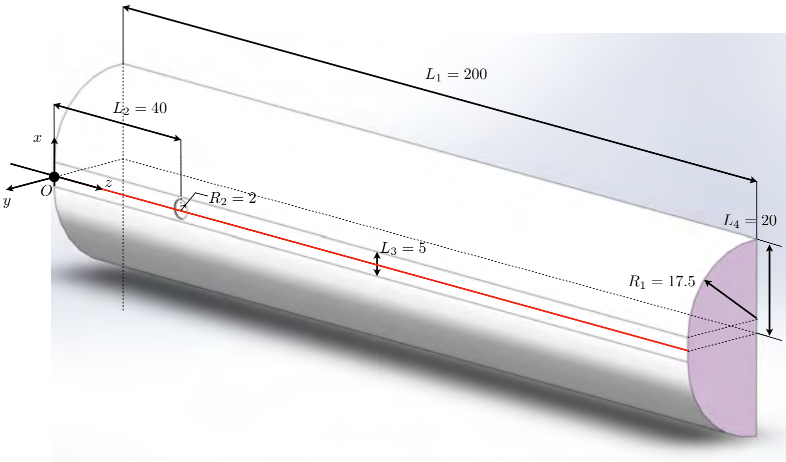

Figure 2: Schematics of the swept blunt leading edge used for numerical simulations.

The computational model comes from recent experimental tests in the FD-07 Mach 6.0 hypersonic wind tunnel of the China Academy of Aerospace Aerodynamics. The experimental model is the front part of a delta wing with a swept angle Λ of 45 degrees. The thickness of the wing is $2L_4 = 40$mm. The spanwise length along the attachment line is 425mm. An asymptotic state can be reached at around half the position of the model. The front part of the wing is polished and can be seen as a plate. In this study, we have established a coordinate system, as in figure 2 wherein the z-axis aligns with the leading edge of the swept blunt model, coinciding with the attachment line and extending in the corresponding spanwise direction. The normal direction on the corresponding attachment line and swept blunt body is defined as the y-axis. Finally, the x-axis is defined to complete the typical Cartesian coordinate system in conjunction with these two axes. As usual, a body fitted coordinate (ξ, η, z) is also established with the same spanwise direction as the Cartesian coordinate system, while the ξ-axis is defined along the chordwise direction and the η-axis is defined along the surface normal directions.

Based on that geometry, a computational model is designed as in figure 2. The computational model can be likened to a sandwich-like configuration, where the top and bottom layers consist of semicircles with a radius of $R_1 = 17.5$mm, and the intermediate layer is a flat plate with a width of 5mm. Together, these three layers form the complete swept blunt body configuration. The roughness elements is located at $z = L_2 = 40$mm, at the center of the leading plate. The radius of the roughness is $R_2 = 2$mm. The length of the whole model is designed as $L_1 = 200$mm. Based on experiments, the surface temperature is set to $T_w^* = 370$K , other relative flow parameters are listed in table 1.

As previous analysis around the attachment-line boundary layers, we define the sweep Mach number M_s and the sweep Reynolds number Re_s as

$$Re_s = \frac{w_\infty^* \delta_r^*}{\nu_r^*} \approx 714, M_s = \frac{w_\infty^*}{c_s^*} \approx 2 \tag{8}$$

Flow conditions	M_∞	Re_∞	T^*_∞	T^*_w	Λ	γ
	6.0	1.8×10^4	56.58K	370K	45^o	1.4
Parameters for roughness elements	S_r	k_h	k_h/δ^*_{bl}	d	Re_{kk}	N_k
case H0100	1.0	0.1mm	≈ 0.5	4mm	≈ 678	≈ 87
case H0200	1.0	0.2mm	≈ 1	4mm	≈ 2776	≈ 125

Table 1: Basic parameters for flow and roughness at basic grid. N_k is the number of wall normal points for $0 \leqslant y \leqslant k_h$. $\delta^*_{bl} = 0.2$mm is the thickness of the laminar boundary layer at the attachment-line boundary layer.

based on the length scale $\delta^*_{al} = \sqrt{\nu^*_r \partial u^*_e/\partial x^*}$ at exact attachment line $x^* = 0$ and the variables outside of the attachment-line boundary layer. c^*_s is the sound speed after the leading shock, ν^*_r stands for the kinematic viscosity at recovery temperature $T^*_r \approx 433K$ and the temperature at the edge of the leading attachment-line boundary layer is $T^*_{at,e} \approx 260K$. The value $\partial u^*_e/\partial x^*$ at exact attachment line $x^* = 0$ is not known a priori for the present case, the potential flow around a circular cylinder with equivalent radius L_4 is thus used to evaluate the derivative. By using the linear stability theory over two dimensional domains, the neutral surface of the most dangerous discrete mode are presented in figure 3 over a $Re_s - M_s - \beta$ coordinate. Detailed settings and calculations can be found in many previous studies[13, 31, 16]. Here, β is the normal spanwise wave numbers. The red line in figure 3 indicates the case we focus on in this study. It is found that the critical Reynolds number increases with increasing sweep Mach number, which indicates that the leading viscous mode (Görtler-Hämmerlin mode) is supressed by the compressible effects. Also, it is clearly shown that the present case (the red line) is locate at the stable or subcritical region, which means that the transition to turbulence at the present case is not triggered by a linear instability.

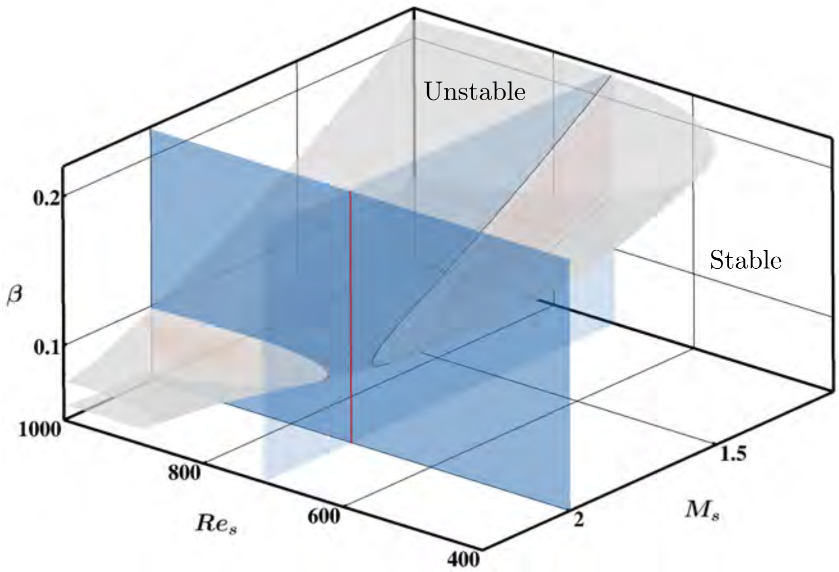

Figure 3: The neutral surface of the most dangerous discrete temporal mode over the $Re_s - M_s - \beta$ plane. The growth rate space is divided into stable and unstable regions by the neutral surface.

2.4 Roughness elements

The roughness element, shown in figure 4, designed to simulate a pressure sensor with a circular disk configuration during the experiment, is characterized by the function expressed in polar coordinates (r, ϕ), with the shape of the shoulders being defined by a hyperbolic tangent function in similar ways as in previous studies[32, 33]. The function is defined as

$$h(r,\phi) = \frac{k_h}{2} + \frac{k_h}{2}\tanh\left[\frac{S_r}{k_h}\left(\frac{d}{2} - r\right)\right], \quad (9)$$

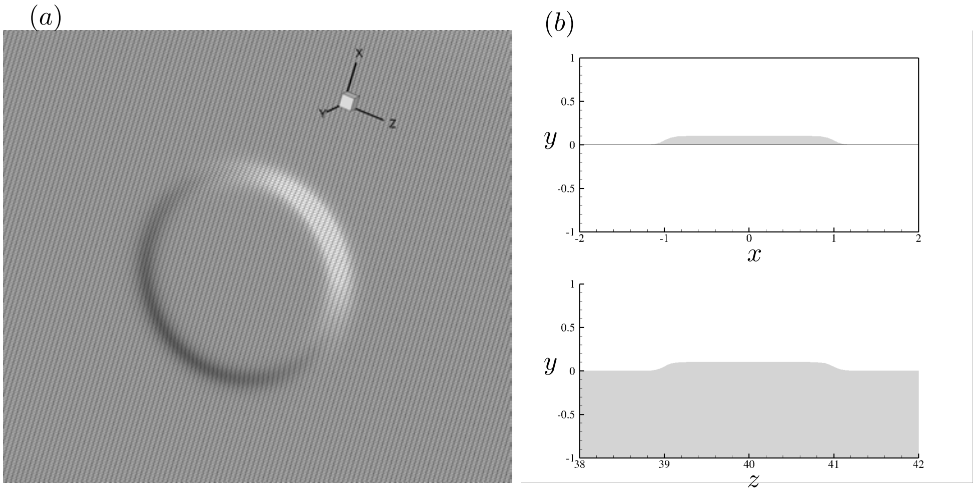

Figure 4: (a) The grid distributions arount the roughness with the roughness height $k_h = 0.1$mm in full resolution. (b) The shape of roughness in two cross sections

with k_h and d being the height and diameter of the roughness. The slope factor S_r is set to 1.0 for all cases in the present study. In general, the center of the roughness is locate at the points $(x_c, z_c) = (0, 40)$, the diameter is $d = 4$.

Another important parameter for roughness induced transition is the Roughness reynolds number Re_{kk}, characterised based on the height (k_h) and the velocity (w) in the undisturbed laminar flow with respect to the position of the roughness. This roughness reynolds number is defined as a function of

$$Re_{kk} = \frac{\rho(k_h)w(k_h)k_h}{\mu(k_h)}, \tag{10}$$

and listed in table 1 based on the laminar boundary layer.

2.5 Simulation strategy

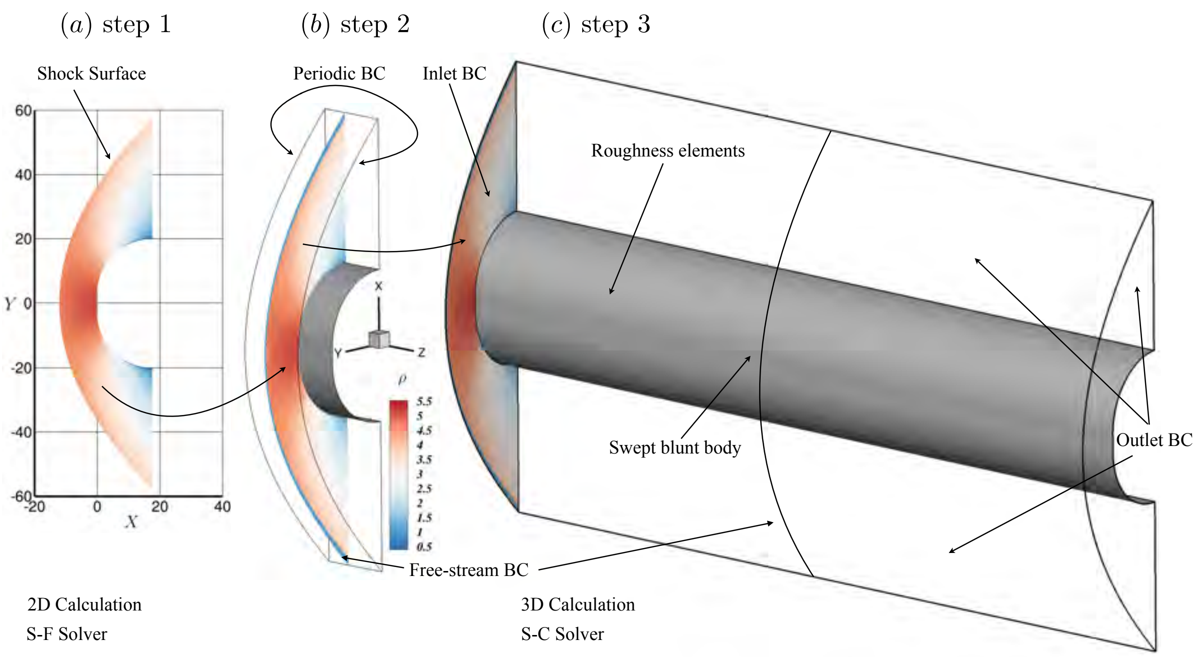

Figure 5: The outline of calculation processes. S-F: Shock Fitting, S-C: Shock Capture

The calculation process for this kind of problem is divided into three steps, with two kinds of compressible solvers[26, 17] as shown in figure 5. Assuming the incoming flow has reached an asymptotic state, a two-dimensional calculation with infinity span assumption ($\partial/\partial z = 0$) is performed first using a shock-fitting solver. With the exact location of the shock revealed, alignment and clustering of the mesh along the bow shockwave can be easily achieved for the following shock-capture calculation. To diminish the numerical perturbations between the two solvers, a three-dimensional domain is further designed for pre-calculation with a periodic boundary condition along the spanwise direction, with the newly built grid and the initial field from the fitting solver. When the calculation is converged, the solution from the middle slice of the periodic three-dimensional domain is used for the fully three-dimensional calculation. As the boundary layer develops along the attachment line and the chordwise direction, non-reflection outlet boundary conditions are used further downstream along the attachment line and the chordwise direction. Away from the surface, as the shock is embeded in the computational domain, freestream boundary conditions are used at the outside.

To closely mimic the conditions observed during experimental tests, the generation of unsteady perturbations is implemented in two distinct phases. In the first phase, random velocity perturbations, with maximum amplitude constituting approximately 2% of the free-stream velocity, are introduced upstream of the leading shock waves. This procedure aims to replicate the perturbations measured in wind tunnel experiments. In the second phase, to simulate the disturbances inherent to upstream boundary layers along the attachment line, random wall normal blowing and suction are executed via a hole on the wall. These disturbances, too, possess an maximum amplitude of roughly 2% of the free-stream velocity. The specified hole is positioned at coordinates $(z_c, x_c) = (30, 0)$ and defined with a radius of 2.

In the computational analyses conducted within the scope of this study, two distinct cases were examined. In the first scenario, characterized by a roughness element height of 0.1mm, unsteady perturbations were deliberately introduced to facilitate the onset of transition. Otherwise, the transition would not occur within the wake flow induced by the roughness elements. Conversely, the scenario involving a roughness element height of 0.2mm presented a fundamentally different dynamic. The inherent absolute instability associated with this configuration led to a spontaneous disruption of flow symmetry. This natural progression towards asymmetry effectively initiates the transition process, obviating the need for the introduction of external perturbations.

To facilitate the analysis investigating the mean field characteristics, both Reynolds-averaged and Favre-averaged mean quantities are employed, following the approach of Huang *et.al*[34]. The Reynolds-averaged mean of an arbitrary variable f is denoted by $\overline{f}$, while the Favre-averaged mean is denoted by $\tilde{f} = \overline{\rho f}/\overline{\rho}$. In addition, the fluctuations around the Reynolds and Favre averages are represented by single and double primes, respectively. That is, $f' = f - \overline{f}$ and $f'' = f - \tilde{f}$. Given the absence of homogeneous directions in the configurations under consideration, achieving ideally averaged states necessitates a considerable amount of time.

The statistical analysis of the flows was conducted over a span of 1800 time units, encompassing approximately 900,000 steps. This duration is roughly ninefold the time required for a flow to evolve from the inlet to the spanwise flow outlet. To ascertain the independence of flow statistics from the duration of statistical analysis, we performed an additional test. This test involved comparing flow statistics derived from two distinct averaging intervals, with one interval containing 50% more statistical steps than the other, to ensure that any discrepancies of the flow statistics for major variables between the two intervals were small enough, not exceeding 0.1%.

3 Results

3.1 General features of the flow fields

The general features of the whole flow fields are shown in figure 6 and figure 7, with the iso-surfaces of $\lambda_2 = -0.035$ transient fields and iso-surfaces are colored with spanwise velocity w. The whole flow fields can be divided into three parts. The first part is the roughness region, in which the initial laminar flow is perturbed by the surface deformation. Typical vortex structures are formed behind the roughness, which can be seen as streaks. The secondary instabilities of streaks and the breakdowns, lead to typical turbulent structures, along the attachment line, and small vortexes structures are shown. The second part is the transitional region, in which the initial turbulences at the attachment line develop along the spanwise direction as well as the chordwise direction. At the very beginning, the turbulences are located around the attachment line and the turbulent region expands along the chordwise direction slightly. Then, as the flows develop further downstream, the turbulent structures are flushed from attachment-line region to chordwise outlet. The final part is the fully turbulent region, where the fully developed

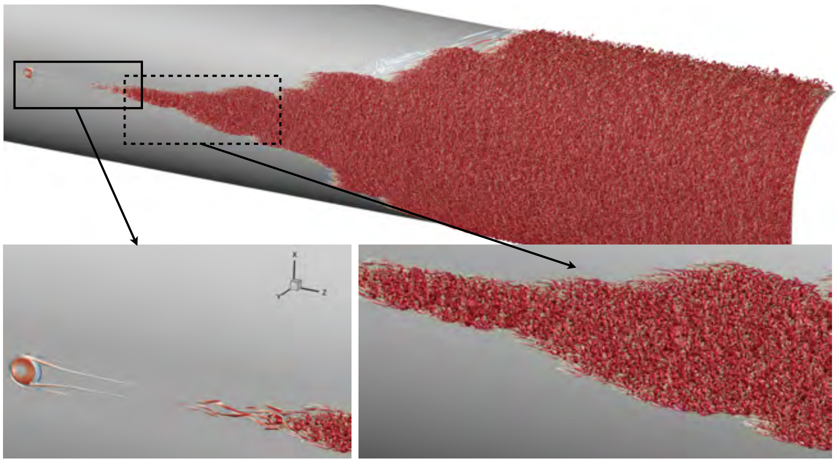

Figure 6: Instantaneous iso-surface of $\lambda_2 = -0.035$, colour indicates w, for the first part of case H0100.

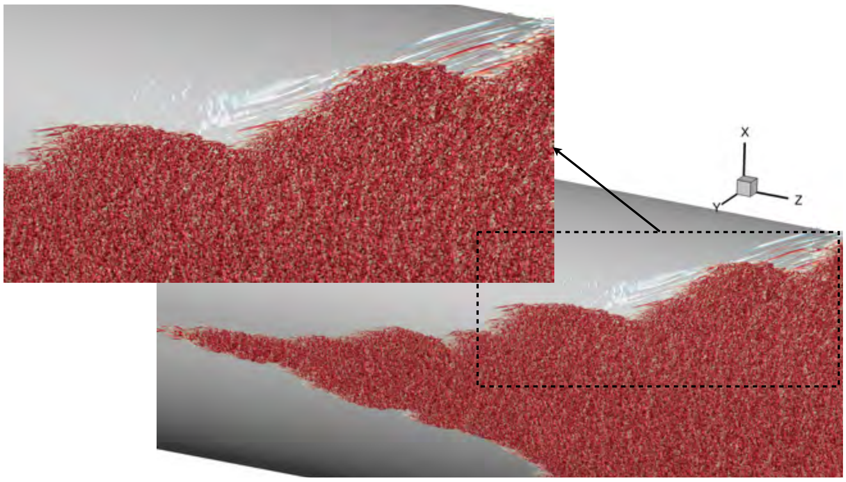

Figure 7: Instantaneous iso-surface of $\lambda_2 = -0.035$, colour indicates w, for the second part of case H0100.

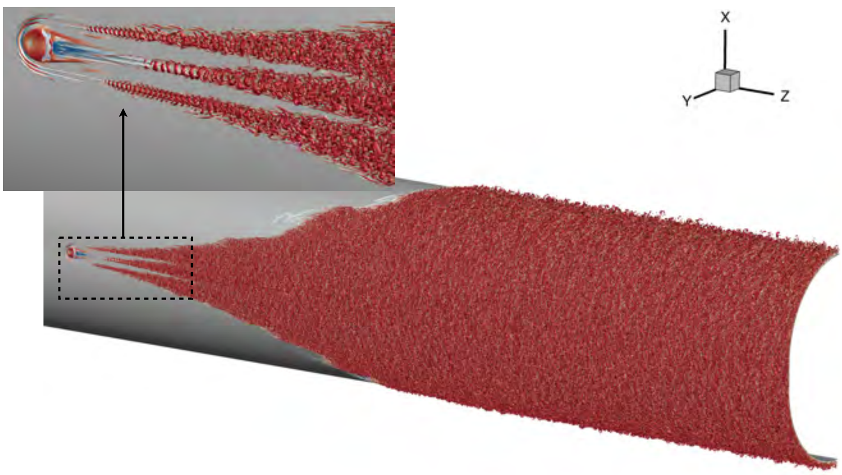

Figure 8: Instantaneous iso-surface of $\lambda_2 = -0.035$, colour indicates w, for the case H0200.

turbulences cover the whole region of the leading-blunt body, ranging from attachment line to chordwise outflow.

When the height of the roughness element is increased from 0.1 to 0.2, there are significant differences in the vortex structures formed behind the roughness, as shown in figure 6 and 8. These differences can be seen more directly in the contours of surface average heat fluxes θ_{tw} and skin frictions $\overline{\tau}_w$, as depicted in figures 9 and 10. These metrics essentially serve as "footprints" of the boundary layer dynamics, providing insights into the complex interactions and flow structures present within the boundary layers. Here, as the usual boundary layers in previously, we define the velocity $\overline{u}^+$, based on inner scale as

$$\left.\begin{aligned} h^+ = \frac{\overline{\rho}_w \overline{u}_\tau h}{\overline{\mu}_w}, \quad \overline{u}^+ = \frac{|\overline{u}_p|}{\overline{u}_\tau}, \quad |\overline{u}_p| = \sqrt{\overline{u}_\xi^2 + \overline{w}^2}, \\ \overline{u}_\tau = \sqrt{\frac{\overline{\tau}_w}{\overline{\rho}_w}}, \quad \overline{\tau}_w = \frac{\overline{\mu}}{Re} \left.\frac{\partial \overline{u}_p}{\partial h}\right|_{h=0}, \end{aligned}\right\}, \tag{11}$$

where, $\overline{u}_p$ is the velocity parallel to the surface. The skin-friction coefficient C_f and surface heat-flux θ_{tw} for this kind of flow are defined as

$$C_f = \frac{2\overline{\mu}_w^*}{\rho_\infty^* U_\infty^{*2}} = \frac{2\overline{\mu}_w}{Re} \frac{\partial \overline{u}_p}{\partial h} = 2\overline{\tau}_w, \theta_{tw} = -\left|\kappa \nabla \overline{T} \cdot \boldsymbol{n}\right|. \tag{12}$$

The derivatives of surface normals, denoted as $\partial/\partial h$, for arbitrary variables f_ψ, are determined through a two-step process. Initially, the gradients of the variables f_ψ are computed utilizing the identical scheme adopted for the calculation of viscous fluxes during the simulations. Subsequently, the derivatives of the surface normals $\partial f_\psi/\partial h$ are obtained by projecting the calculated gradients ∇f_ψ onto the surface normal vectors $\boldsymbol{n}$.

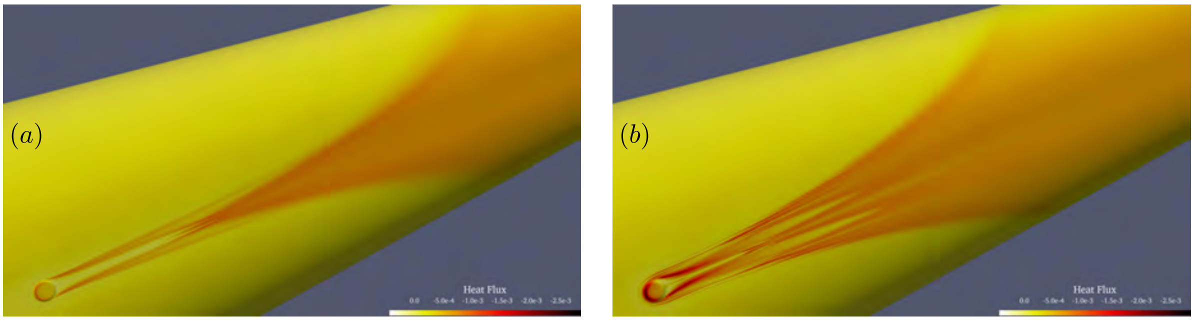

Figure 9: The surface heat fluxes distributions for two cases. (a) for H0100, (b) for H0200.

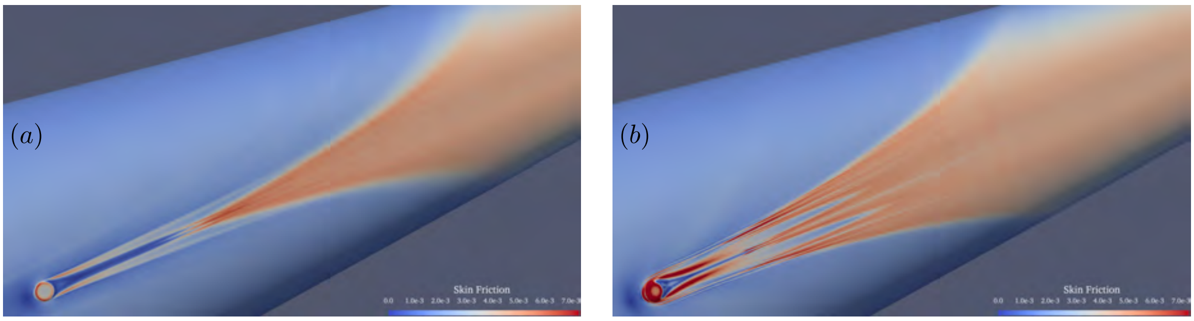

Figure 10: The surface skin friction distributions for two cases. (a) for H0100, (b) for H0200.

The magnitude contour of average density gradients for case H0200, at the attachment-line plane, is depicted in figure 11. This illustration provides a comprehensive view of the general flow field characteristics for both cases. The presence of surface roughness induces a shock slightly ahead of the roughness. As this shock evolves away from the surface and progresses downstream, it shapes into a curved shock surface under the influence of the incoming flow. The interaction of this induced shock with the leading shock of the blunt body, followed by its reflection back into the boundary layer downstream, results in a noticeable deformation of the leading shock. Subsequent to the roughness-induced shock, the compressed fluids undergo expansion and acceleration, leading to the formation of a recompression shock at the roughness's tail along the $z-$direction. Meanwhile, a shear layer develops behind the roughness, and the recompression shock once again impinges on the leading shock, reflecting back into the boundary layers. When the flow evolves further downstream, the high-shear region at the outside of the boundary layer becomes much weak, as reflected as the decrease of magnitudes for the density gradient $|\nabla\rho|$.

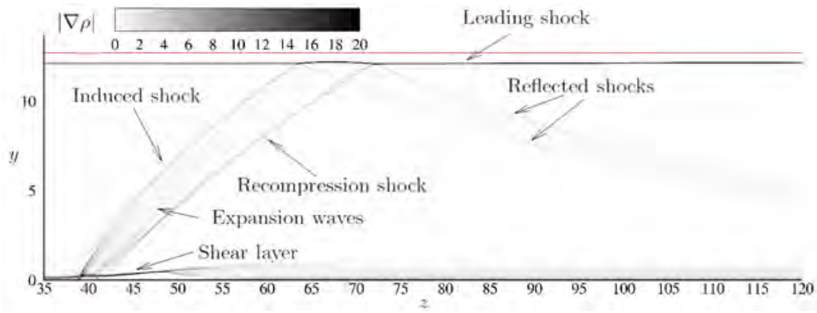

Figure 11: Density gradient magnitude contours of the case H0200, at attachment-line plane $x = 0$. The red line stands for the computational domain.

The figure 12 and 13 show the distributions of mean velocity and temperature along the attachment line in the wall-normal direction. Additionally, the size and specific location of the corresponding separation bubbles are indicated by blue lines in the figures. It is evident from the figure that the separation bubbles induced by small roughness elements are lower in height compared to those induced by large roughness elements, but extend farther downstream. Conversely, the separation bubbles induced by larger roughness elements extend farther upstream. The corresponding velocity and temperature profiles highlight the approximate location of the shear layer and illustrate the process through which low-speed fluid, due to the lift-up effect, is elevated away from the wall.

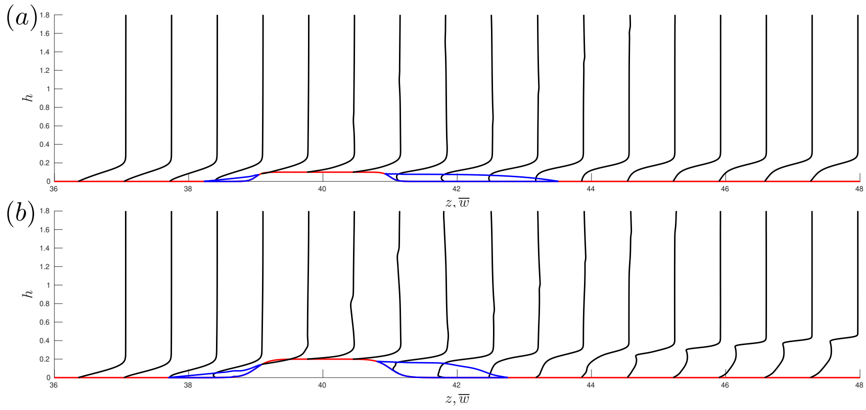

Figure 12: Line plots of average spanwise velocity $\overline{w}$ around the roughness for (a) H0100 and (b) H0200 cases. The red and blue lines stand for the wall surfaces and seperation bubbles, respectively.

3.2 Mechanisms of the roughness induced transition

In this section, we try to understand the transition mechanisms of these flows by using long time one-point spectra statistics. At the beginning, all sampled points are located at the attachment-line plane($x = 0$). Figure 14 and 15 show the instantaneous flow fields at the exact attachment-line plane for the two cases, together with the statistical results of the selected points. The regions of the revease flow near the roughness are pointed by the white lines. As mentioned previous, the two distinct cases deliver two different dynamics with respect to the transition processes. In the first scenario, case H0100, the transition would not occur within the wake flow induced by the roughness elements, without the unsteady perturbations, even though the roughness Reynolds number Re_{kk} or the height of the roughness k_h are beyound the critical values in normal plate boundary layers[35, 36, 37]. Contrariwise, as the height of

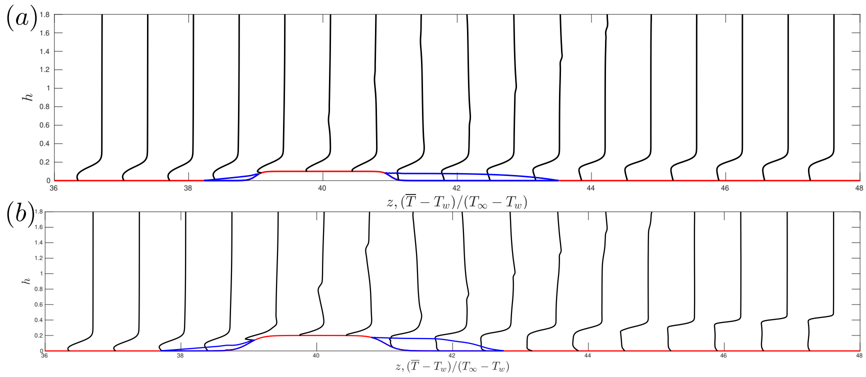

Figure 13: Line plots of average Temperature $(\overline{T} - T_w)/(T_\infty - T_w)$ at the attachment line around the roughness for (a) H0100 and (b) H0200 cases. The red and blue lines stand for the wall surfaces and seperation bubbles, respectively.

roughness element increases to 0.2, the transition will occur without employing forcing of any kind, which suggest a self-sustaining mechanism that causes the flow to transition.

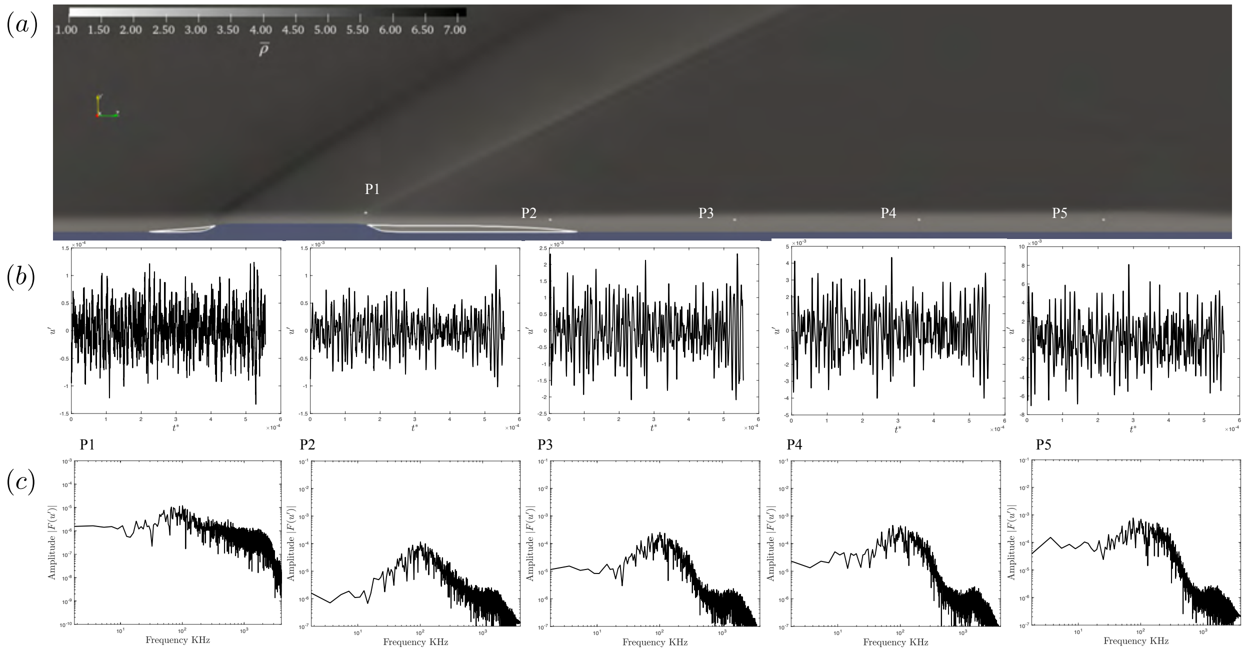

Figure 14: (a) The instantaneous density contour at the attachment-line plane $x = 0$ for case H0100. (b) The temporal evolutions of instantaneous chordwise velocity perturbations u' of the selected points. (c) The amplitudes for different Fourier modes $|F(u')|$ for different frequency at the selected points.

This is also reflected in the corresponding measurement point signals of u'. In H0100 case, we introduced random perturbations, resulting in the signal detected at point P_1 exhibiting typical broadband characteristics, with energy distributed relatively uniformly across a range of frequencies. Additionally, there is a slight increase in perturbation amplitude at the frequency around 70 KHz. As the flow continues to develop downstream from P_2 to P_5, the perturbations gradually increase, and disturbances around the frequency around 70 KHz become the dominant perturbations. This leads to the frequency amplitude distribution characteristics evolving towards typical turbulent features.

When the height of the roughness element increases to 0.2 mm, prominent instability waves are observed at points P_1, P_2 and P_3. The figures indicate that the disturbances, which are amplified as they travel downstream from P_1 to P_3, not only grow in a convective manner but also exhibit characteristics of absolute instability, as they are amplified over time at fixed locations. Based on the results of the discrete Fourier transformation, the frequency of the most representative perturbations is around

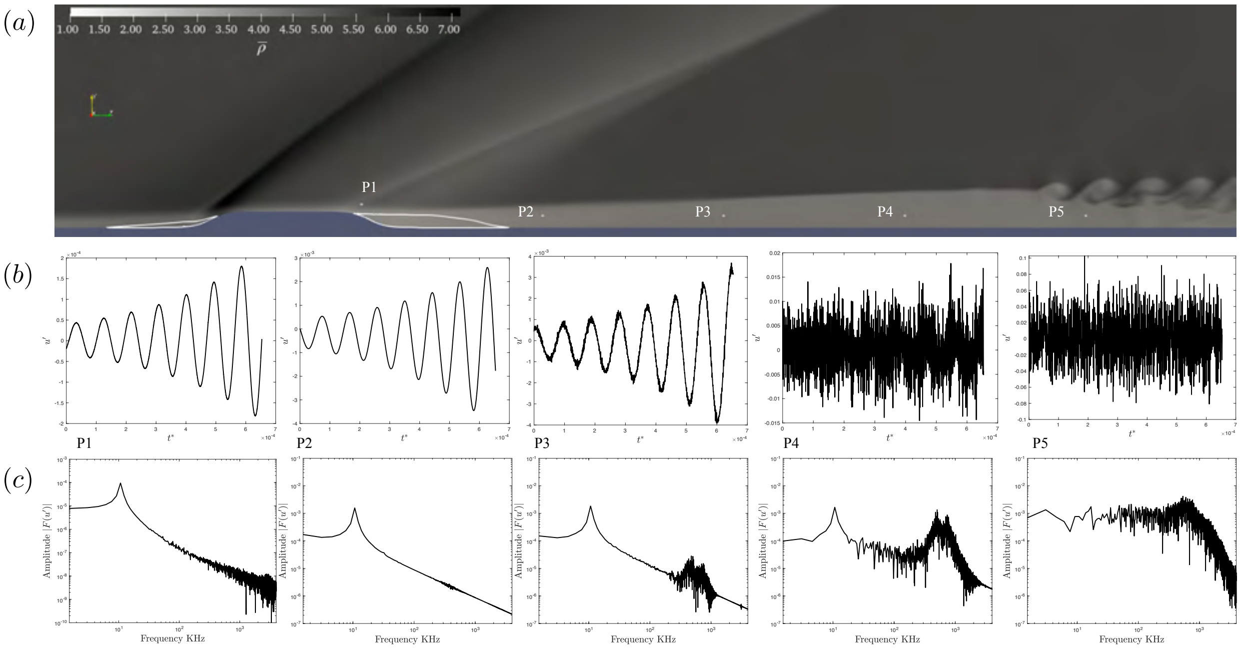

Figure 15: (a) The instantaneous density contour at the attachment-line plane $x = 0$ for case H0200. (b) The temporal evolutions of instantaneous chordwise velocity perturbations u' of the selected points. (c) The amplitudes for different Fourier modes $|F(u')|$ for different frequency at the selected points.

10 KHz, referred to as low-frequency perturbations in this study. As these perturbations evolve downstream, some high-frequency components are gradually amplified. This amplification is evidenced by the increasing amplitude of disturbances in the region beyond 400 KHz. Simultaneously, the low-frequency perturbations appear to reach a saturation state as they evolve downstream, with their amplitude showing minimal growth. This is evidenced by the nearly constant amplitude of low-frequency disturbances from points P_2 to P_4 in the figures. As the flow continues to develop further downstream to point P_5, the overall disturbance spectrum exhibits typical broadband characteristics which indicates that the flow are stepping into full turbulent.

To better understand the mechanisms and identify possible nonlinear coupling features during the transition processes, higher-order spectral (HOS) analysis is employed. Specifically, bispectral analysis is utilized here to examine nonlinear signals. This method enables the detection and quantification of possible nonlinear interactions between different frequency components of the signals. The bispectrum $\mathscr{B}(\omega_1, \omega_2)$ for a signal $f(t)$ is defined as

$$\mathscr{B}(\omega_1, \omega_2) = E\left[\mathscr{F}(\omega_1)\mathscr{F}(\omega_2)\mathscr{F}^c(\omega_1 + \omega_2)\right], \tag{13}$$

where $\mathscr{F}(\omega)$ is the Fourier transform of the temporal signal $f(t)$ and ω is the frequency. $E[.]$ stands for an expected value. The superscript c represents the complex conjugate.

The bispectrum of selected points in figure 14 and 15 are shown in figure 16 and 17, respectively. For both cases, the most representative interactions between two waves with different frequencies are shown. Based on the definition of bispectrum (13), it measures the nonlinear interactions between frequencies ω_1 and ω_2, as well as their sum $\omega_1 + \omega_2$. For a purely linear signal, the bispectrum theoretically should be zero or very close to zero. For general nonlinear signal, the diagonal elements (if $\omega_1 = \omega_2 = \omega_0$) of the bispectrum reflect the interactions between a frequency ω_0 with itself and its double frequency $2\omega_0$. Significant values along the diagonal often indicate the presence of harmonic components in the signal. The off-diagonal elements (if $\omega_1 \neq \omega_2$) illustrate the nonlinear interactions between distinct frequencies ω_1 and ω_2, and their sum frequency $\omega_1 + \omega_2$. The obvious values off the diagonal suggest the nonlinear coupled phenomena between different frequency components.

The basic behaviour of the perturbations, shown in figure 16 and 17, are the same as described before. For the H0100 case, the results indicate that regions with larger magnitudes of low-frequency disturbances are primarily located on or near the diagonal. This suggests that in this condition, the excitation of higher-order harmonics plays a significant role in the nonlinear evolution of the corresponding

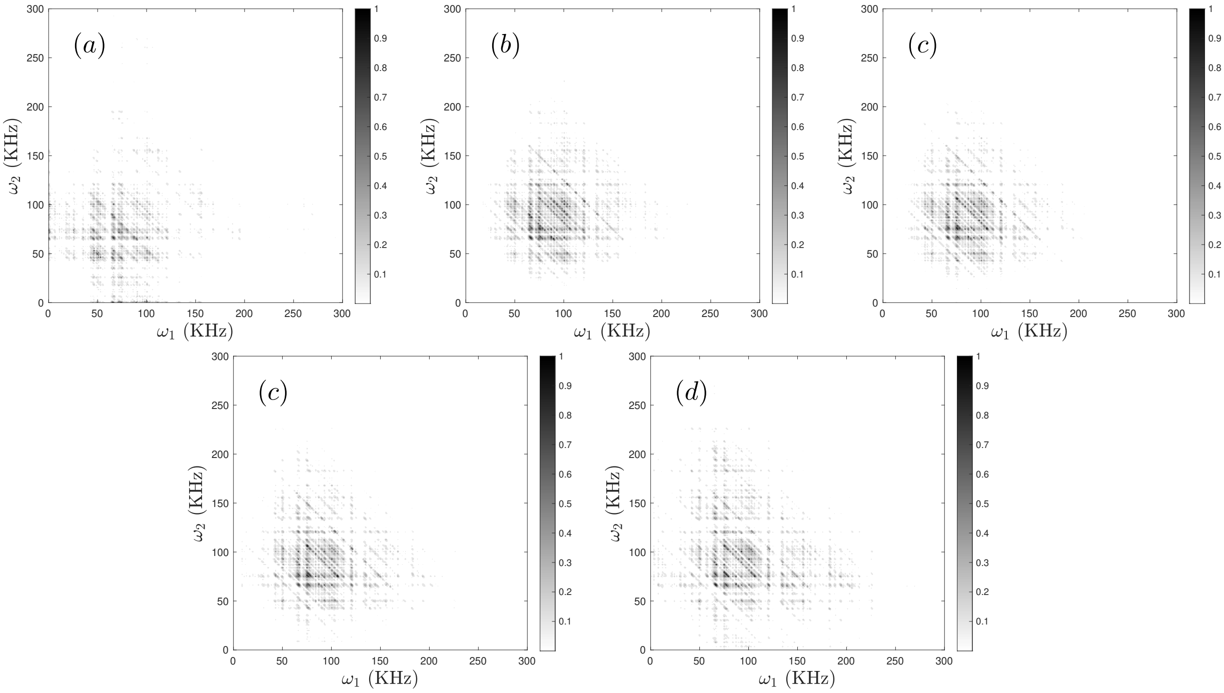

Figure 16: The normalized bispectrum $|\mathscr{B}|$ of the perturbations u' at the points P_1 to P_5 for the H0100 case. Panels (a) to (d) correspond to points P_1 to P_5, respectively.

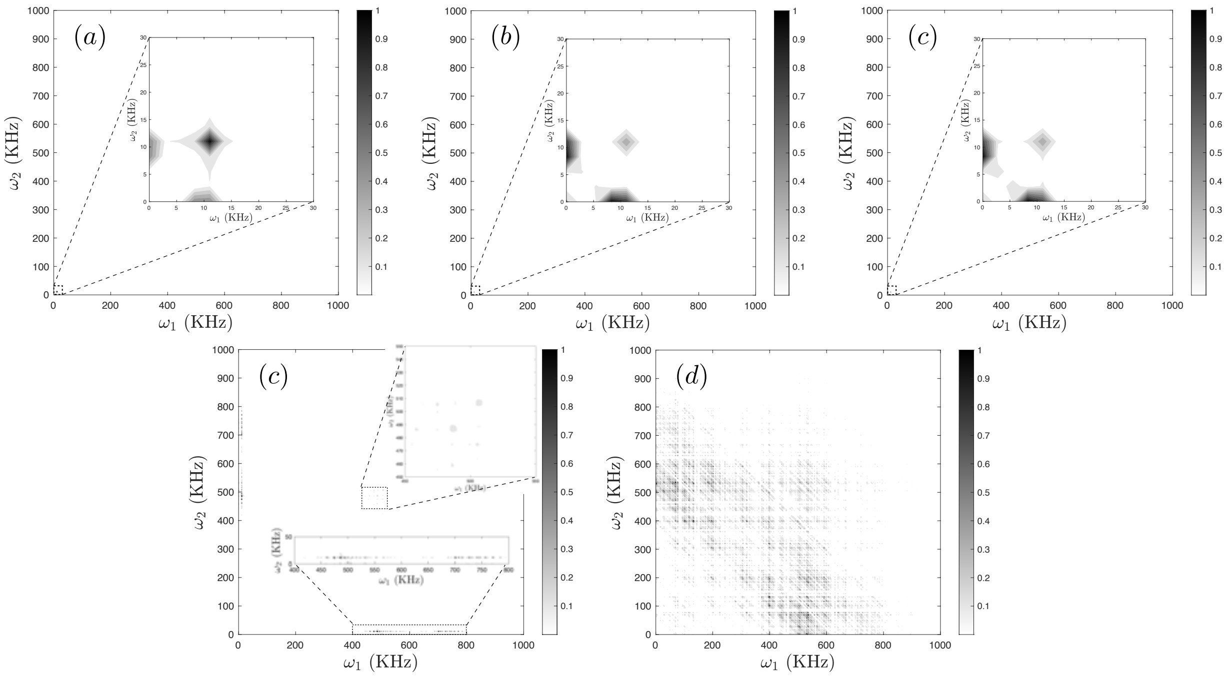

Figure 17: The normalized bispectrum $|\mathscr{B}|$ of the perturbations u' at the points P_1 to P_5 for the H0200 case. Panels (a) to (d) correspond to points P_1 to P_5, respectively. Note that certain features have been magnified for enhanced readability and clarity.

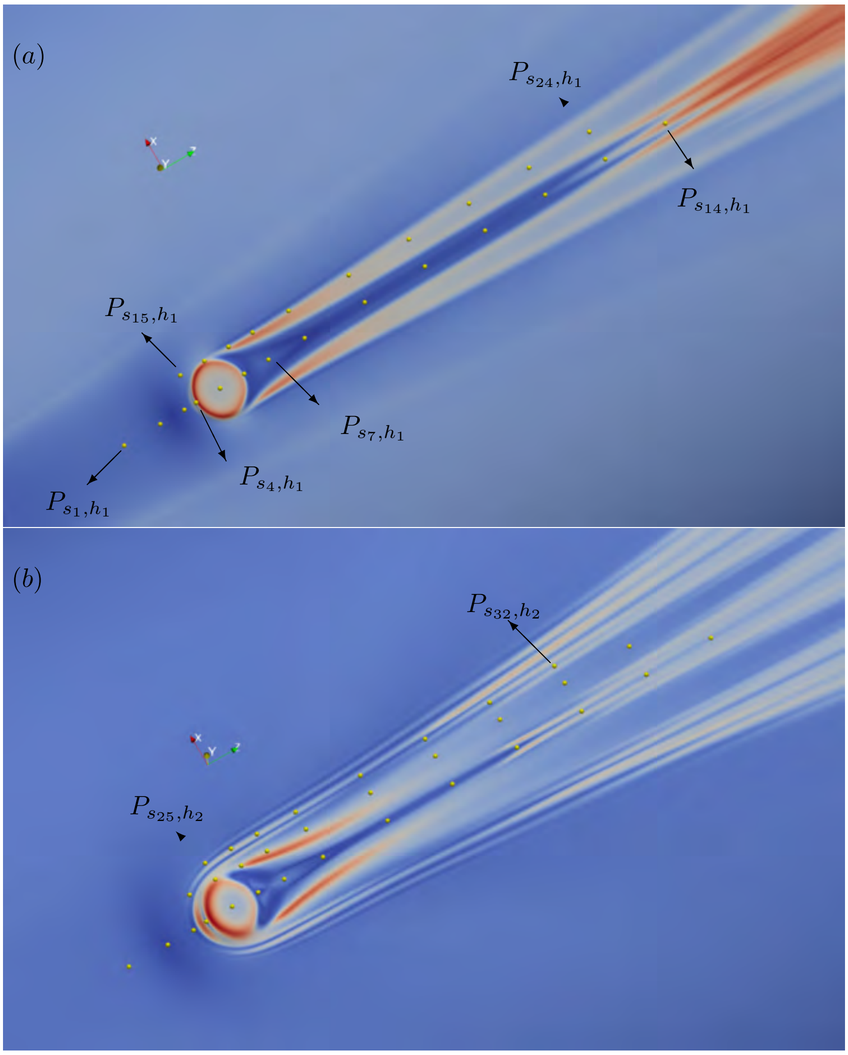

Figure 18: The selected points for two cases. (a) for H0100, (b) for H0200. The corresponding points are sequentially recorded as $s_1, s_2, \cdots, s_{32}$ along the z-axis from upstream to downstream, starting from the attachment line to chordwise downstream. The subscripts h_1 and h_2 are used to distinguish the points in different cases.

disturbances. As the disturbances propagate downstream, the spectral distribution of disturbances at points P_2 through P_4 appears to remain relatively unchanged. This indicates that the composition of the disturbances remains nearly constant, suggesting that the disturbances have grown to a certain extent and have reached a nearly saturation stage.

For the H0200 case, the bispectrum exhibits characteristics that are markedly different from the previous condition. At the first three signal recording points (P_1, P_2, and P_3), the dominant disturbances in the overall disturbance spectrum appear only in the low-frequency region, consistent with the results from the previous power spectrum analysis. As the disturbances further develop to point P_4, some high-frequency disturbances begin to emerge, roughly within the $[400\mathrm{KHz}, 800\mathrm{KHz}]$ range. These high-frequency disturbances exhibit significant nonlinear interactions with the low-frequency disturbances as well as the zero-frequency disturbances, with the frequencies of the low-frequency disturbances remaining consistent with those recorded at the previous three points. This suggests that the low-frequency disturbances have evolved sufficiently, and the detected high-frequency disturbances correspond to a secondary instability arising in the already saturated low-frequency disturbances combined with the mean field.

To provide a more comprehensive understanding of the disturbance evolution process during transition, we shift our focus slightly away from the wake of roughness elements at the attachment-line region to analyze the characteristics of disturbance evolution around the entire roughness element, including the upstream and horseshoe vortex regions. In order to trace the evolution characteristics of disturbances in the three-dimensional flow field, we select and record the fluctuating density on the three-dimensional

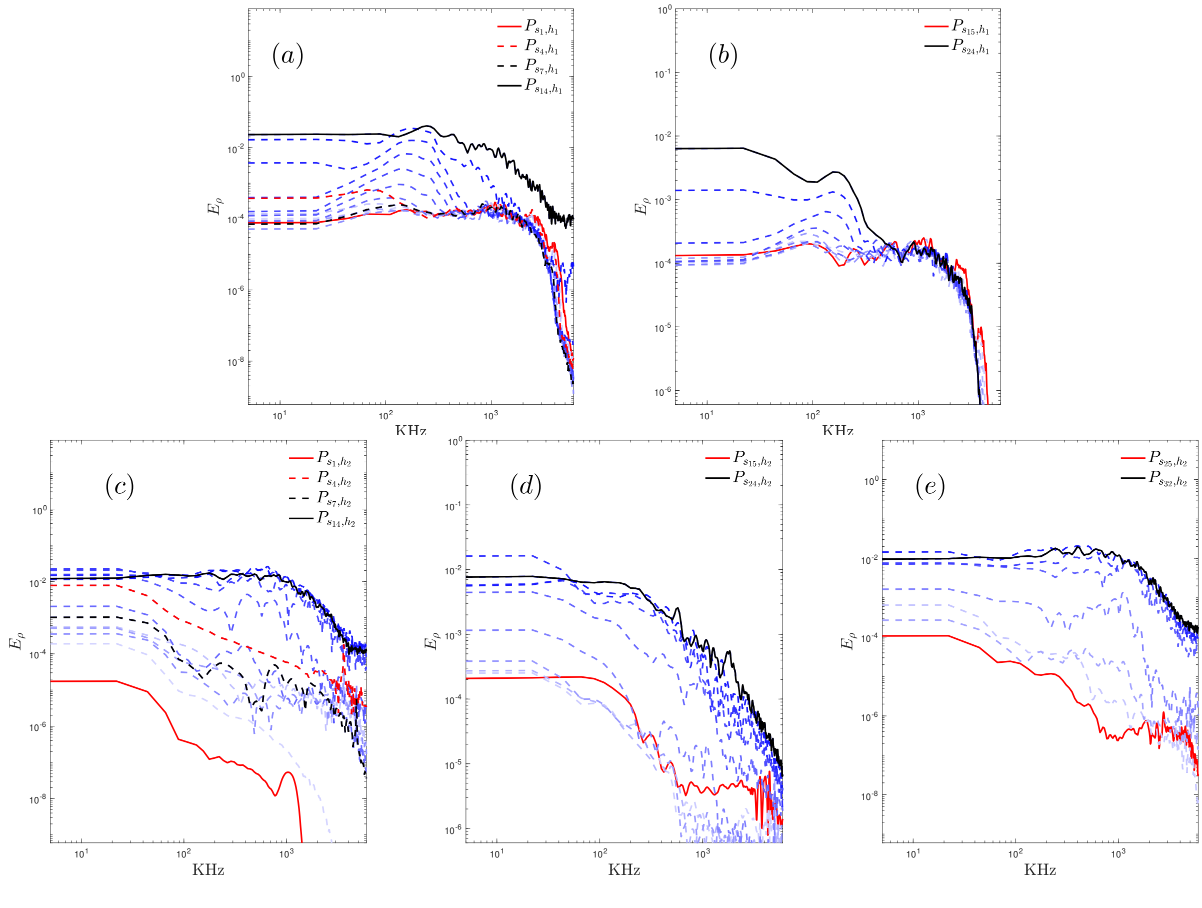

Figure 19: The spectra E_ρ of perturbations density ρ at the selected points in figure 18. (a) and (b) stand for the two groups of selected points in H0100 case. $(c-e)$ represent the three groups of selected points in H0200 case. From light to dark blue dashed lines, the spectra represent points from spanwise upstream to downstream.

surfaces around the roughness element for analysis. The selected points for H0100 and H0200 cases are shown in figure 18 together with the surface skin friction. The selected points can roughly be divided into three groups. The first group is located along the exact attachment line, extending from upstream to downstream of the roughness element, labeled sequentially as $s_1, s_2, \cdots, s_{14}$. The second group is located on the side of the roughness element, also extending from upstream to downstream, labeled as $s_{15}, s_{16}, \cdots, s_{24}$. The third group, labeled as $s_{25}, s_{26}, \cdots, s_{32}$, is also on the side of the roughness element but is further from the second group of detection points. The first two groups are the same for both cases, while the third group appears only in the H0200 case to track the evolution of the corresponding horseshoe vortex.

The spectra of those points are shown in figure 19. In the scenarios of lower height roughness element, the incoming flow ahead of the roughness is subjected to the additional perturbations. Based on the spectra(the red lines in figure 19(a) and (b)), no dominant frequency could be observed. As the flow gradually approaches the roughness element, the overall amplitude of disturbances increases progressively (as indicated by the red dashed line in Figure 19(a)). After the fluid passes over the roughness element, the disturbances are somewhat suppressed due to the adverse pressure gradient resulting from the expansion effects of the high-pressure region induced by the shock wave. This suppression leads to a decrease in the amplitude of the disturbances (as indicated by the black dashed line in Figure 19(a)). However, once the flow moves past the roughness element, the disturbances exhibit a marked tendency to increase again. It is important to note that the frequency range of disturbances that first starts to grow significantly is approximately 100 KHz, which is consistent with previous analyses. As for the vortex structures formed on both sides of the roughness element, they also exhibit similar patterns of change (as indicated in Figure 19(b)). However, the corresponding amplitudes have not grown significantly large (i.e., a distinct plateau region appears in the mid-to-low frequency range), which correlates with the previous observation that no significant transition phenomena were observed on both sides.

In scenarios involving a higher roughness element, different phenomena are observed (as shown in Figures 19($c-e$)). Due to the absence of additionally introduced artificial disturbances under this condition, the amplitude of disturbances upstream of the roughness element is relatively low, especially in the mid-to-high frequency range. As the disturbances approach the roughness element, the amplitude of low-frequency components is generally amplified. Additionally, within the separation bubbles both upstream and downstream of the roughness element, some peaks appear in the high-frequency range (indicated by the red dashed line and black dashed line, where the red dashed line represents the upstream separation bubble and the black dashed line represents the downstream separation bubble), reflecting the high-frequency characteristics of the separation bubbles. Similar to the lower roughness element, disturbances exhibit a certain degree of suppression after passing over the roughness element (the amplitude corresponding to the black dashed line is relatively low). As the flow further moves downstream, disturbances in the high-frequency range gradually increase, resulting in some peaks (these peaks correspond to the high-frequency range identified in previous analyses), eventually leading to fully developed disturbances and the transition to turbulent flow. On the side stimulated by the horseshoe vortex generated by the higher roughness element, similar characteristics are observed, as shown in Figure 19(e). As indicated by the previous analysis of wall heat flux and skin friction, there exists a relatively 'quiet' zone between the two transition peaks (as shown in Figure 19(d)). The corresponding disturbance amplitude in this region is smaller compared to the regions on either side. The disturbances in this zone only begin to grow once the disturbances on both sides have fully developed.

3.3 Mode decompositions of the transitional flow fields

In this section, we aim to understand the transition mechanisms of these flows using two- and three-dimensional mode decompositions. Given the extensive computational grid involved, documenting every instantaneous signal throughout the entire flow domain is virtually impossible. Therefore, to analyze specific flow characteristics, we strategically focused on capturing variable signals within targeted regions to reveal the featured flow structures. Even though regarding the analysis of three-dimensional flow fields, it is important to acknowledge that the significant disk storage requirements for time-sequential data make it impractical to achieve the same level of precision across a broad frequency range as that obtained from one-point statistics analysis. Therefore, we intend to primarily utilize modal decomposition analysis to investigate the potential occurrence of high-frequency disturbances and the three-dimensional structural characteristics of secondary instabilities. The sub-block regions shown in figure **??** are used to record the instantaneous signal of basic variables. The resolutions ($Ns_\xi \times Ns_\eta \times Ns_\zeta$) of the blocks for case H0100 and H0200 are $201 \times 301 \times 801$ and $401 \times 301 \times 701$, respectively. Additionally, 600 time samples are recorded at a time step of $\Delta t = 0.1$, covering a total of 60 basic time units.

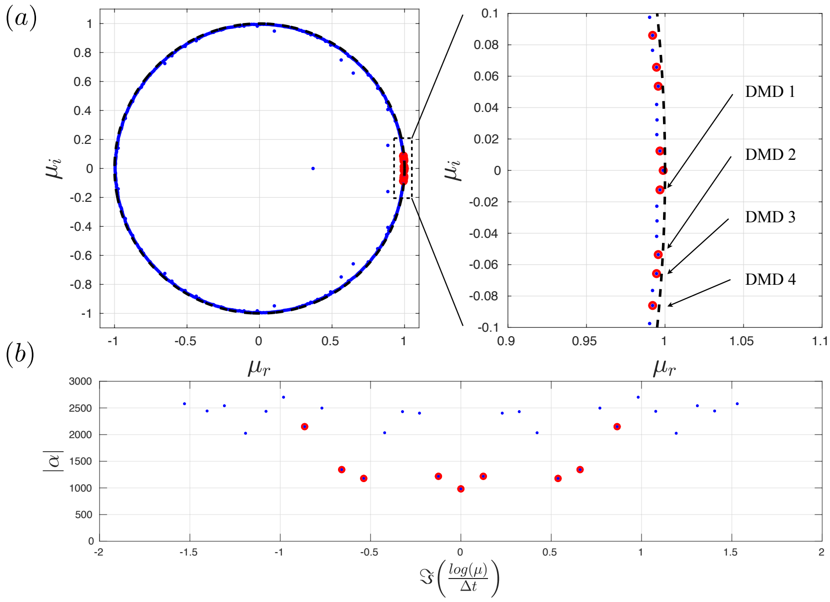

Figure 20: The spectrum and selected modes of DMD for H0100 case in three-dimensional region. The λ_2 is used as observation variable. (a) shows the spectrum. (b) shows the frquency $\Im(\log(\mu)/\Delta t)$ and amplitude $|\alpha|$.

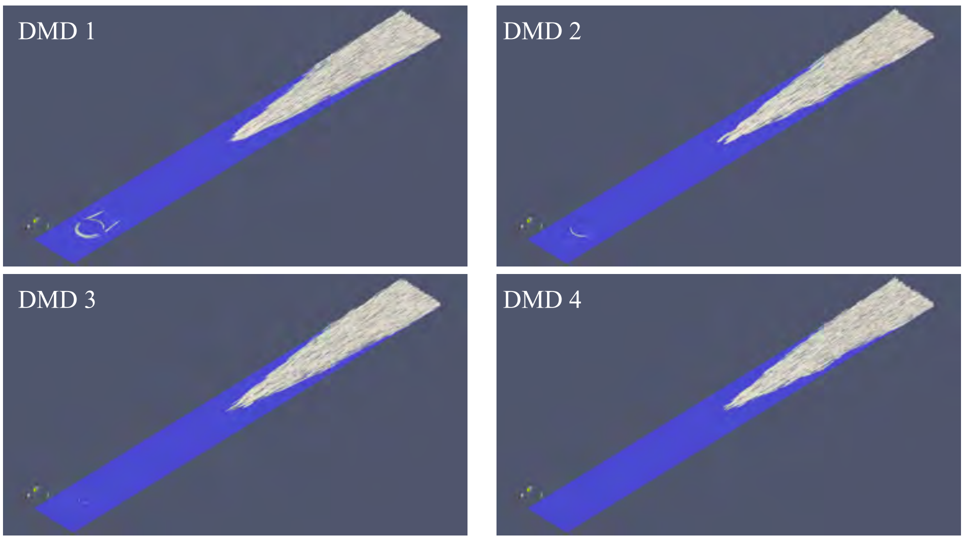

Figure 21: Spatial structures of the selected DMD modes with iso-surfaces of $\lambda_2 = -5 \times 10^{-5}$, for case H0100.

In approximating the Koopman eigenfunctions of continuous systems associated with nonlinear NS equations through dynamic modes, selecting appropriate variables becomes crucial for generating significant spatio-temporal patterns. Koopman theory suggests that good observables might better capture the dynamics of nonlinear systems. Consequently, this study employs the λ_2, a variable derived from vortex identification, serving as a dynamic indicator for structures. The decomposition's fundamental parameters are detailed in Table 2. Due to the prohibitive size of the input datasets, necessitating distributed memory high-performance computing, this work adopts and adapts a parallelized algorithm, as described by Sayadi & Schmid [38], to facilitate DMD.

The DMD results for case H0100 are shown in figure 20 and 21. The most important modes are shown in the spectrum. Excluding the associated mean flow mode, the selected dominant modes all exhibit distinct streak characteristics. The corresponding disturbance structures are primarily distributed downstream of the roughness elements, highlighting the feature that in the later stages of transition

Case	Observations	Ns_ξ	Ns_η	Ns_ζ	Dof	No. (snapshots)	Memory (Tb)
H0100	λ_2	201	301	801	0.48×10^8	600	0.22
H0200	λ_2	401	301	701	0.85×10^8	600	0.4

Table 2: Basic parameters of domains and the observations used for the decomposition. Degree of freedom(Dof) stands for the variables numbers per snapshots. Memory represents the memory requirements for storing all input data.

and in turbulent states, higher-frequency disturbances gradually become more prominent. Additionally, the decomposed Modes 1, 2, and 3 all display significant disturbance characteristics near the roughness elements. This indicates that the transition is not simply and spontaneously occurring at a certain downstream distance from the roughness elements, but is instead connected with the upstream disturbances near the roughness elements.

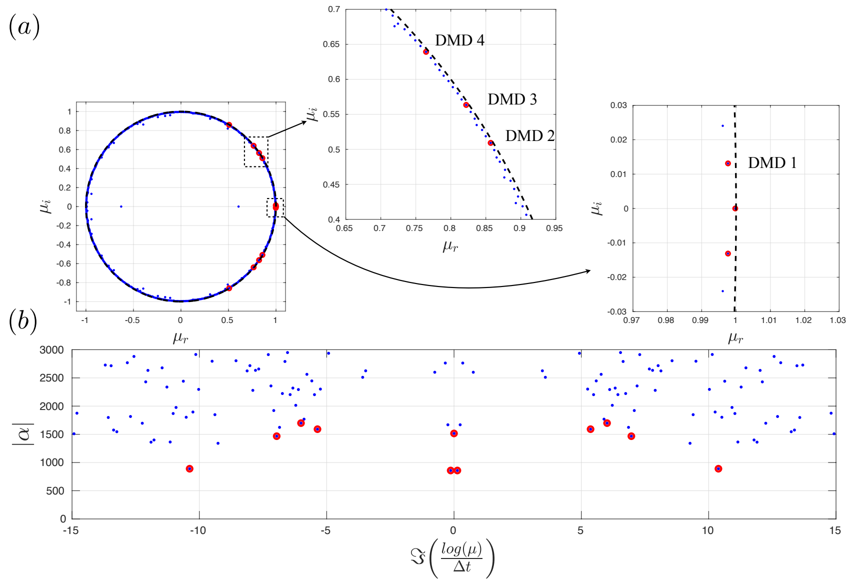

Figure 22: The spectrum and selected modes of DMD for H0200 case in three-dimensional region. The λ_2 is used as observation variable. (a) show the spectrum. (b) shows the frquency $\Im(\log(\mu)/\Delta t)$ and amplitude $|\alpha|$.

The results of case H0200 are presented in figure 22 and 23, which exhibit distinct differences compared to case H0100. The Mode 1 exhibits typical streak structures, however, unlike previous conditions, in addition to the streaks at the central position (around $x = 0$), there are also streak regions on either side. These lateral regions correspond to the vortex structures formed at the edges of the larger roughness elements, continuing their downstream development. Modes 2, 3, and 4 reflect the flow structures known as hairpin vortices in the typical transitional boundary layer induced by roughness elements. These structures represent the intense momentum mixing processes occurring during transition. These modes clearly illustrate that at certain distances from the stagnation line, the flow streaks evolving from the upstream horseshoe vortex enter a strong nonlinear phase earlier than those along the centerline, forming corresponding vortex structures.

3.4 The features of three-dimensional turbulent boundary layers

In this section, boundary-layer profiles are extracted at several locations from the present simulations for H0200 case, and the local turbulence statistics are shown to give a relative complete and comprehensive understanding of the turbulent features in the present three-dimensional configurations.

Prior to addressing the issues of turbulence, it is crucial to ensure that the flow has reached a fully developed turbulent state. Therefore, we perform spectral analysis on the fluctuation data obtained from points selected along the attachment-line plane. The procedure for computation of the frequency spectrum follows the method discussed by Choi & Moin[39]. The 60000 time snapshots with time

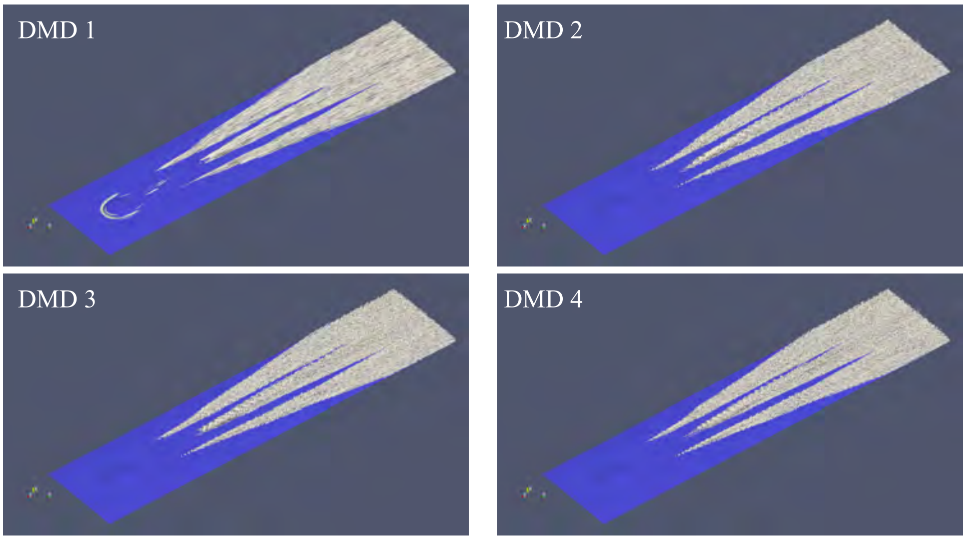

Figure 23: Spatial structures of the selected DMD modes with iso-surfaces of $\lambda_2 = -5 \times 10^{-5}$, for case H0200.

step $\Delta t = 0.01$ are divided into overlapping segments, each containing 5000 sample points. Figure 24 shows the frequency spectrum E_u of the velocity fluctuations u' at several spanwise locations along the attachment line. From the figure, it can be observed that the spectra of fluctuations at different positions nearly overlap, indicating that the fluctuations at these two positions have very similar characteristics. The spectra also reflect typical scaling laws consistent with turbulence statistics, such as the well-known -5/3 slope. However, it should be noted that the Reynolds number of the turbulent boundary layer in this study is not high, resulting in a limited inertial subrange in the spectrum. At higher wavenumbers, the dissipation spectrum aligns well with Heisenberg's -7 scaling[40]. All these ensure that the flow has reached a state of fully developed turbulence.

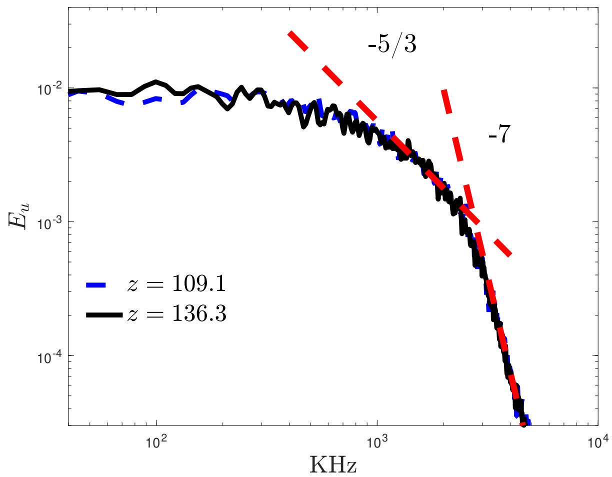

Figure 24: The frequency spectrum of the perturbations u' at several spanwise locations along the attachment line. The two dashed red lines stands for the lines $E_u \sim -5/3$ and -7.

The transformed mean velocity profiles are shown in figure 25. $(a) - (i)$ represents the locations along chordwise directions, range from the exact attachment line to downstream chordwise direction. The transformed mean velocity profiles w^+_{VD}, w^+_{TL}, w^+_{V} and w^+_{ts} are shown to assess the ability in collapsing mean velocity profiles in compressible three-dimensional boundary layers on the incompressible law-of-the-wall. Firstly, we look at the profiles at the exact attachment line(Figure 25(a)). Excluding the Trettel & Larsson transformation, the other three transformations yielded satisfactory results. There were two unexpected findings: First, based on previous research, the Trettel & Larsson transformation is expected to perform well in fully developed, non-spatially varying boundary layers; however, in the conditions investigated in this study, it inaccurately predicted the logarithmic region. Second, it is well-

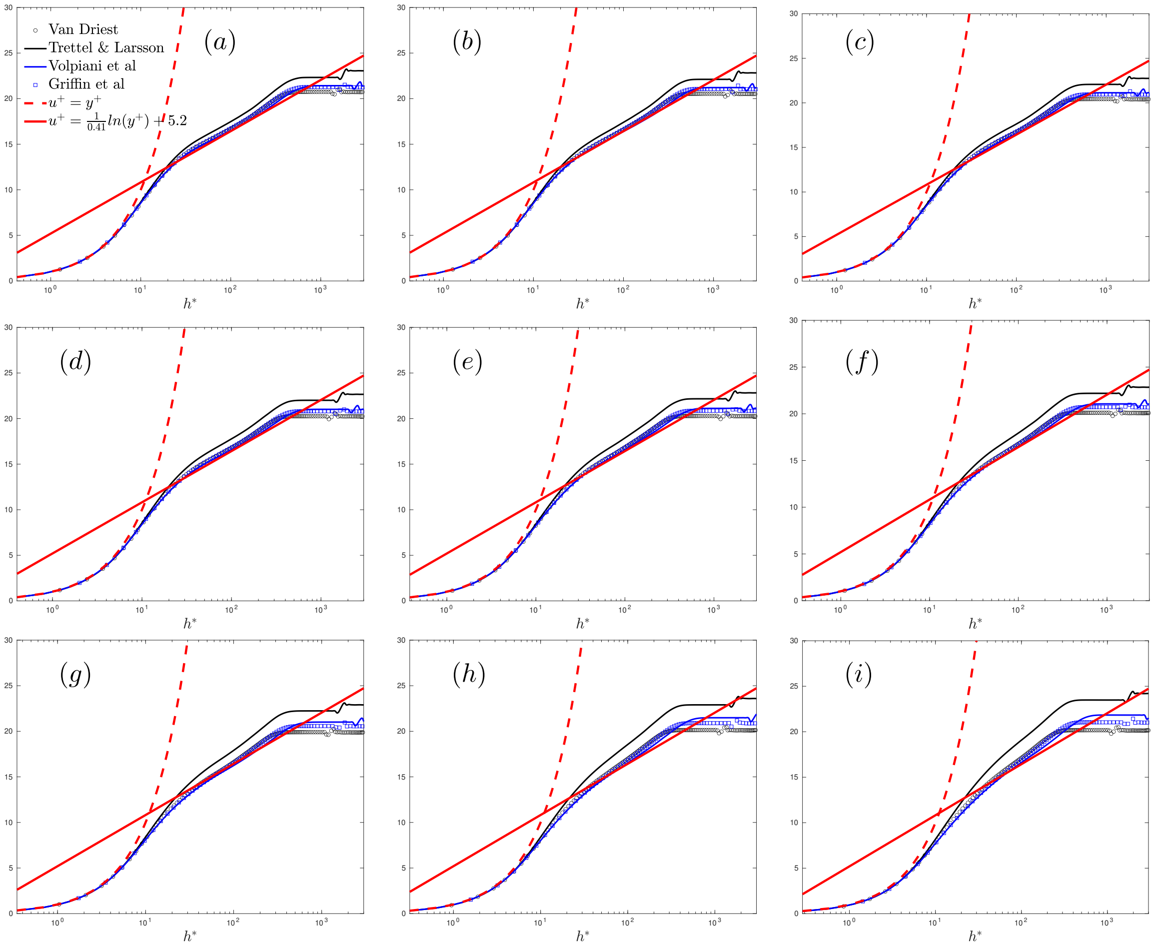

Figure 25: Mean velocity profiles of spanwise velocity $\overline{w}$ along the the wall normal direction at selected locations along the surface. $(a) - (i)$ stands for the locations range from the exact attachment line to downstream chordwise direction.

known that the Van Driest transformation generally performs poorly in compressible, heat-exchanging flat-plate turbulent boundary layer flows. Nevertheless, under the conditions of this study, the Van Driest transformation produced acceptable results.

As the position gradually moves away from the attachment line to the point of maximum transverse pressure gradient (Figure 25(f) and (g)), different velocity transformations continue to exhibit similar patterns to those observed at the attachment line. This indicates that in the present fully developed three-dimensional turbulent compressible boundary layer, even in the presence of transverse pressure gradients and transverse velocity components, the mainstream velocity component still largely conforms to the velocity transformations previously established for flat-plate boundary layers.

The temperature profiles also play a vital role in compressible boundary, therefore, the widly used relationship between the mean velocity and mean temperature is also shown to assess the scaling relations in three-dimensional boundary layers. The mean temperature-velocity relation model given by Zhang $et.al$[41], which is also known as the generalized reynolds analogy, is defined as

$$\left.\begin{aligned} \frac{\overline{T}}{T_e} &= \frac{T_w}{T_e} + \frac{T_{rg} - T_w}{T_e}\frac{\overline{u}_p}{\overline{u}_{p,e}} + \frac{T_e - T_{rg}}{T_e}\left(\frac{\overline{u}_p}{\overline{u}_{p,e}}\right)^2, \\ T_{rg} &= T_e + \frac{r_g \overline{u}_{p,e}^2}{2C_p}, r_g = \frac{2C_p(T_w - \overline{T}_e)}{\overline{u}_{p,e}^2} - 2Pr\frac{\theta_{tw}}{\overline{u}_{p,e}\overline{\tau}_w}, \end{aligned}\right\}, \tag{14}$$

where the subscript e stands for the variables at the edge of boundary layer and the velocity $\overline{u}_p$ represents the velocity parallel to the local surface. Figure 26 show the compaisons of the average temperature-velocity relations. Under the corresponding conditions, it can be observed that when the crossflow velocity is relatively low, the relationship between the mean velocity parallel to the wall $\overline{u}_p$ and the

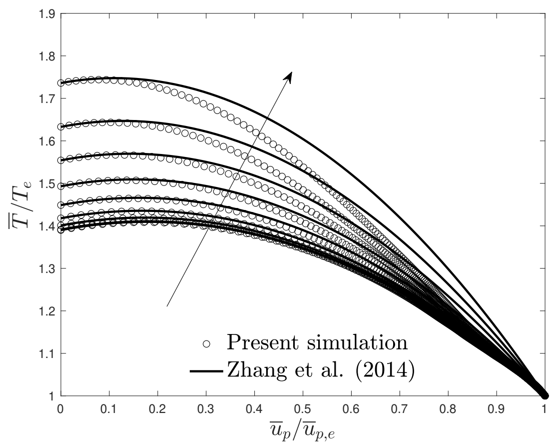

Figure 26: Comparison of the average temperature-velocity relations from simulations and generalized reynolds analogy. From bottom to top, the positions successively correspond to the downstream locations along the chordwise direction from the exact attachment line.

mean temperature $\overline{T}$ still conforms to the corresponding temperature-velocity relation, with acceptable error margins. However, when the crossflow velocity increases beyond a certain threshold, significant discrepancies arise between the temperature-velocity relation applicable to two-dimensional flows and the numerical simulation results.

Based on the hypothesis given by Morkovin, transformations for reynolds stresses $\widetilde{u_i''u_j''}$,

$$\left.\begin{aligned} (u_i^*)^2 &= \frac{\overline{\rho}}{\overline{\rho}_w}\frac{\widetilde{u_i''^2}}{\overline{u}_\tau^2}, \quad i=1,2,3 \\ (u_iu_j)^* &= \frac{\overline{\rho}}{\overline{\rho}_w}\frac{\widetilde{u_i''u_j''}}{\overline{u}_\tau^2}, \quad i\neq j \end{aligned}\right\}, \tag{15}$$

are used to shown the basic profiles along the wall normal directions and the essential features are expected to follow the incompressible form. The profiles are presented as a function of the semilocal scaling h^*. The results of a incompressible turbulent boundary layer at $Re_\tau = 445$ simulated by Jiménez $et.al$[42] and a compressible turbulent boundary layer at $Re_\tau = 453$ simulated by Cogo $et.al$[43] are used as references.

The reynolds stresses along the wall normal directions at the positions, from the exact attachment line to further chordwise directions are shown in figure 27. As we anticipated, the computed and statistically analyzed Reynolds stresses at and near the exact attachment line (figure 27(a)-(c)) agree well with the results obtained from direct numerical simulations (DNS) for both incompressible and compressible flat-plate boundary layers. The peak values and shapes of the Reynolds stresses in the streamwise direction are consistent with the corresponding reference values. This agreement validates the resolution of our current computational. However, the Reynolds stresses in the wall normal and chordwise directions are smaller than the reference values. This discrepancy is likely due to the influence of the leading-edge shock wave and the spanwise pressure gradient in the conditions of this study. At the leading edge, the height of the shock wave from the wall is approximately 13 mm, which is about six times the turbulent boundary layer thickness at that location. This suppresses the development of fluctuations in this direction, resulting in lower corresponding Reynolds stresses $(v^*)^2$. Along the chordwise direction at the leading edge, the condition $d/dx = 0$ is satisfied only at the exact attachment line, hence the Reynolds stresses $(u^*)^2$ in this direction are also somewhat suppressed. As the flow develops to further downstream locations along the chordwise direction, the spanwise Reynolds stresses $(w^*)^2$, exhibit an obvious decrease. However, this decrease of intensity along the spanwise direction do not reflect the actual variations of intensity of turbulence. The real strength of turbulence can be identified in the turbulent kinetic energy, , $K = 0.5\widetilde{u_i''u_i''}$, (see figure 28). It can be observed that as the position moves in the chordwise direction away from the attachment line, the turbulent intensity first experiences a slight increase followed by a decrease. This reflects the combined effects of enhanced shear caused by the three-dimensional nature of the flow field and the favorable pressure gradient along the chordwise direction.

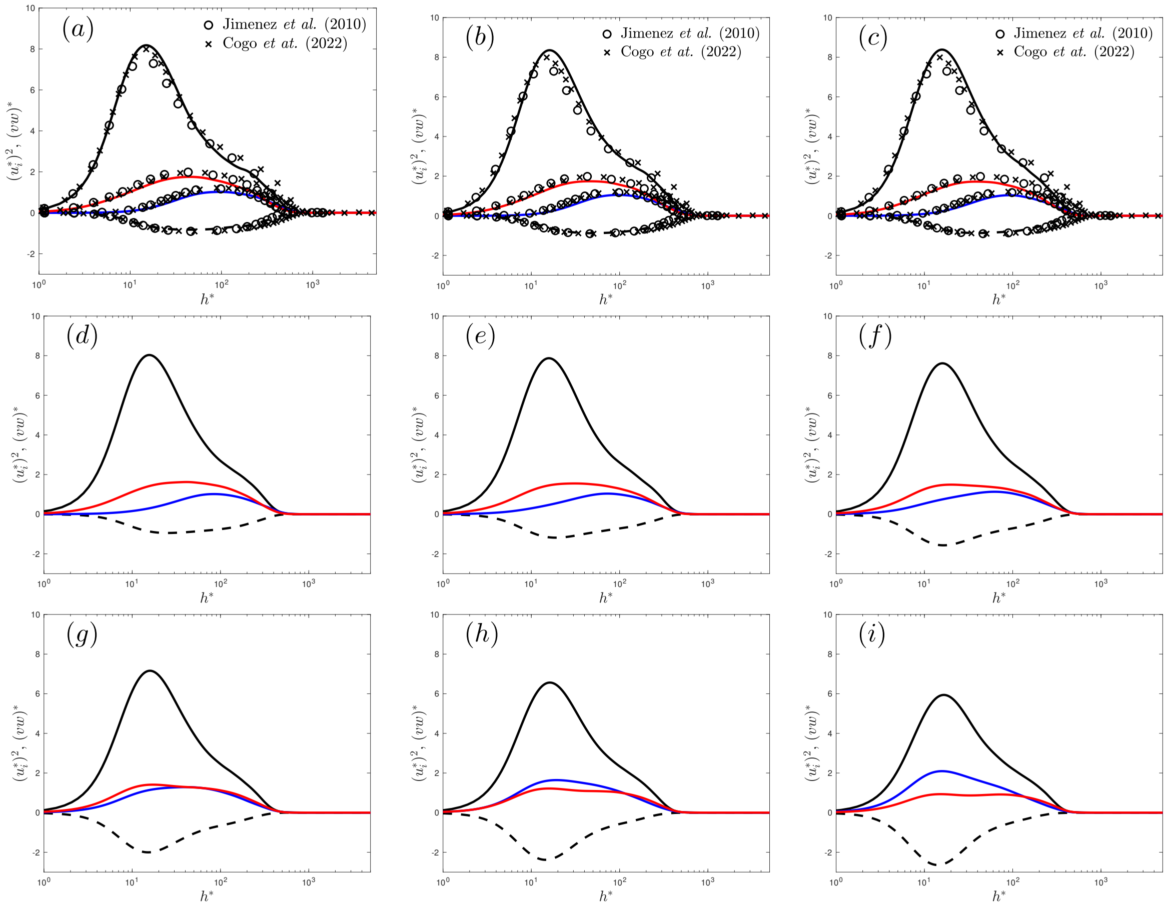

Figure 27: The reynold stress distributiones along the wall normal direction. The solid black, red and blue lines stand for the $(w^*)^2, (v^*)^2$ and $(u^*)^2$, respectively. The dashed line stands for $(vw)^*$. $(a) - (i)$ stands for the locations range from the exact attachment line to downstream chordwise direction.

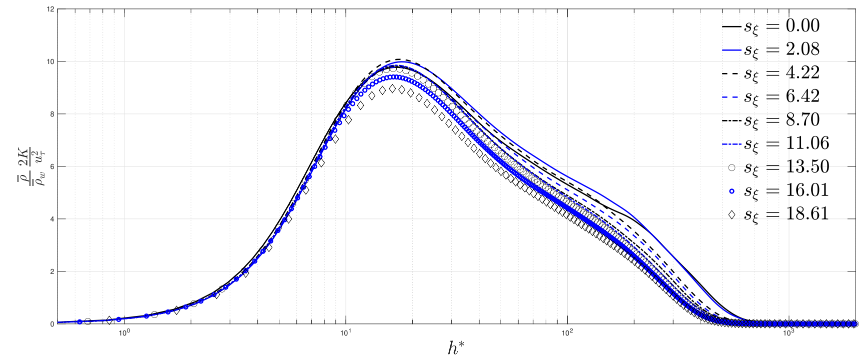

Figure 28: The distributions of the normalized turbulent kinetic energy at chordwise positions s_ξ.

4 Conclusions

In this research, numerical simulations of roughness induced high-speed attachment-line boundary layers over a real blunt configuration, without the infinity-span assumptions are performed. Based on linear stability theory, the subcritical state of the possible transition along the attachment line is confirmed. Two roughnesses based on the experimental tests are modeled and designed to trigger transitions. The main findings of this study can be summarized as the following four points

- In the flow over a swept blunt body discussed in this paper, even without the assumption of infinite sweep, if the incoming boundary layer reaches an asymptotic state (for laminar flow) or a fully developed turbulent state, the subsequent flow state also satisfies the infinite sweep assumption—the boundary layer is homogeneous along the swept direction.

- The two different heights of roughness elements in the configuration studied in this paper result in completely different transition characteristics. For lower-height roughness element, the element alone cannot directly induce the corresponding boundary layer transition. Certain random perturbations need to be introduced during the simulation. For higher-height roughness element, it can directly induce boundary layer transition by themselves without the need for additional perturbations. The flow near the roughness elements resembles that of a flat plate boundary layer, where vortex structures are triggered in their vicinity. In the transition phenomena induced by external disturbances and lower-height roughness elements, the transition mainly occurs directly downstream of the wake of the roughness elements, but the wake vortices induced by the roughness elements do not directly destabilize and lead to the final transition. In the transition simulation with higher-height roughness element, the horseshoe vortices generated by the roughness elements form corresponding streaks, which preferentially destabilize and lead to the transition to turbulence, while the wake vortices directly behind the roughness elements destabilize and transition further downstream.

- One-point power spectral analysis and bispectral analysis, together with the DMD analysis, are used to identify the detailed transition mechanism. For the case of small roughness element, the wake flow induced by the roughness act as a disturbance selector and amplifier, selecting and amplifying the incoming disturbances from upstream. This causes disturbances with frequencies around 70 KHz to preferentially grow and lead to the final transition. Through DMD analysis, we can infer that the high frequency instability is strongly linked to the separation bubble upstream of the roughness elements. For larger roughness elements, there exists a low-frequency absolute instability in the wake induced by the roughness elements. This low-frequency disturbance, around 10 KHz, generates corresponding low-frequency streaks, and the high frequency secondary instability of these low-frequency streaks is the primary reason for the transition in the wake.

- This study further analyzes the complete later-stage transition and the final turbulent processes of a three-dimensional attachment-line boundary layer. When the turbulent boundary layer is fully developed, it is found that the spanwise velocity still conforms to the law-of-the-wall even under conditions with crossflow and pressure gradients. Among several commonly used transformations, all but the Trettle & Larsson transformation yield satisfactory results, bringing the velocity profiles back to those of an incompressible flow. In cases with moderate crossflow velocity, the temperature-velocity transformation relationship retains a good predictive accuracy, but this relationship becomes unsuitable when the crossflow velocity increases significantly. The analysis of the anisotropic Reynolds stress tensors and the turbulent kinetic energy balance indicates that the fundamental characteristics of the three-dimensional turbulent boundary layer remain consistent with those of the two-dimensional turbulent boundary layer.

Acknowledgements

We acknowledge Yancheng MetaStone Tech. Co. for prociding us with the computational resources required by this work. Useful discussions with Professor Chunxiao Xu and Professor Qibing Li of Tsinghua University and Professor Jie Ren of Beijing Institute of Technology and Dr. Jian Liu of China Aerodynamics Research and Development Centerare gratefully acknowledged. We appreciate the support and resources provided by Supercomputing Center in Yancheng and particularly acknowledge the helps and contributions of Dr. Bowen, Yan and Prof. Guangwen Yang of Tsinghua University. We also appreciate

Dr. Dehua, Zhu and Dr. Xinguo, Sha of China Academy of Aerospace Aerodynamics for performing the experimental wind tunnel tests.

Funding

This work received support from the NSFC Grants 12202242, 12172195 and 12388101. The authors are also grateful for the support from the National Key Research and Development Plan of China through project no. 2019YFA0405201, the National Key Project GJXM92579 and the Grants 20231001 in Supercomputing Center in Yancheng.

References

[1] L. Rosenhead. *Laminar Boundary Layers*. Oxford University Press, New York, 1 edition, 1963.

[2] H. Schlichting and K. Gersten. *Boundary-Layer Theory*. Springer-Verlag Berlin Heidelberg, Berlin Heidelberg, 9 edition, 2017.

[3] D. I. A. Poll. Transition in the infinite swept attachment line boundary layer. *Aeronautical Quarterly*, 30(4):607–629, 1979.

[4] P. Hall, M. R. Malik, and D. I. A. Poll. On the stability of an infinite swept attachment line boundary layer. *Proceedings of the Royal Society of London. A. Mathematical and Physical Sciences*, 395(1809):229–245, 1984.

[5] V. Theofilis. On linear and nonlinear instability of the incompressible swept attachment-line boundary layer. *Journal of Fluid Mechanics*, 355:193–227, 1998.

[6] V. Theofilis, A. V. Fedorov, D. Obrist, and U. W. E. Ch. Dallmann. The extended gortler hammerlin model for linear instability of three-dimensional incompressible swept attachment-line boundary layer flow. *Journal of Fluid Mechanics*, 487:271–313, 2003.

[7] P. R. Spalart. Direct numerical study of leading-edgy contamination. In *Proc. AGARD Symp. Fluid Dynamics of Three-Dimensional Turbulent Shear Flows and Transitions*, Çesme, Turkey, 1988. AGARD CP-438.

[8] M. Gaster. On the flow along swept leading edges. *Aeronautical Quarterly*, 18(2):165–184, 1967.

[9] D. Arnal, J. C. Juillen, J. Reneaux, and G. Gasparian. Effect of wall suction on leading edge contamination. *Aerospace Science and Technology*, 1(8):505–517, 1997.

[10] D. Obrist, R. Henniger, and L. Kleiser. Subcritical spatial transition of swept hiemenz flow. *International Journal of Heat and Fluid Flow*, 35:61–67, 2012.

[11] M. O. John, D. Obrist, and L. Kleiser. Stabilisation of subcritical bypass transition in the leading-edge boundary layer by suction. *Journal of Turbulence*, 15(11):795–805, 2014.

[12] M. O. John, D. Obrist, and L. Kleiser. Secondary instability and subcritical transition of the leading-edge boundary layer. *Journal of Fluid Mechanics*, 792:682–711, 2016.

[13] V. Theofilis, A. V. Fedorov, and S. S. Collis. *Leading-Edge Boundary Layer Flow (Prandtl's Vision, Current Developments and Future Perspectives)*, book section Chapter 7, pages 73–82. Solid mechanics and its applications. Springer, Dordrecht, 2006.

[14] F. Li and M. Choudhari. *Spatially Developing Secondary Instabilities and Attachment Line Instability in Supersonic Boundary Layers*. Aerospace Sciences Meetings. American Institute of Aeronautics and Astronautics, 2008.

[15] C J. Mack, P J. Schmid, and J L. Sesterhenn. Global stability of swept flow around a parabolic body: connecting attachment-line and crossflow modes. *Journal of Fluid Mechanics*, 611:205–214, 2008.

[16] Y Xi, J Ren, and S Fu. Hypersonic attachment-line instabilities with large sweep mach numbers. *Journal of Fluid Mechanics*, 915:A44, 2021.

[17] Y Xi, J Ren, L Wang, and S Fu. Receptivity and stability of hypersonic leading-edge sweep flows around a blunt body. *Journal of Fluid Mechanics*, 916:R2, 2021.

[18] A V. Fedorov and I V. Egorov. Instability of the attachment line boundary layer in a supersonic swept flow. *Journal of Fluid Mechanics*, 933:A26, 2022.

[19] I E. Beckwith and J J. Gallagher. Local heat transfer and recovery temperatures on a yawed cylinder at a mach number of 4.15 and high reynolds numbers. Report R104, Langley Research Center, 1959.

[20] T. R. Creel, I. E. Beckwith, and F. J. Chen. *Effects of wind-tunnel noise on swept-cylinder transition at Mach 3.5*. Fluid Dynamics and Co-located Conferences. American Institute of Aeronautics and Astronautics, Atlanta, 1986.

[21] F. J. Chen, T. R. Creel, and I. E. Beckwith. Transition on swept leading edges at mach 3.5. *Journal of Aircraft*, 24(10):710–717, 1991.

[22] A. S. Skuratov and A. V. Fedorov. Supersonic boundary layer transition induced by roughness on the attachment line of a yawed cylinder. *Fluid Dynamics*, 26(6):816–822, 1991.

[23] A. Murakami, E. Stanewsky, and P. Krogmann. Boundary-layer transition on swept cylinders at hypersonic speeds. *AIAA Journal*, 34(4):649–654, 1996.

[24] X. L. Zhong. High-order finite-difference schemes for numerical simulation of hypersonic boundary-layer transition. *Journal of Computational Physics*, 144(2):662–709, 1998.

[25] X. L Chen, Y Xi, J Ren, and S Fu. Cross-flow vortices and their secondary instabilities in hypersonic and high-enthalpy boundary layers. *Journal of Fluid Mechanics*, 947:A25, 2022.

[26] X L. Li, D. Fu, and Y. Ma. Direct numerical simulation of hypersonic boundary layer transition over a blunt cone. *AIAA Journal*, 46(11):2899–2913, 2008.

[27] X .Liang, X L. Li, D. Fu, and Y. Ma. Effects of wall temperature on boundary layer stability over a blunt cone at mach 7.99. *Computers & Fluids*, 39(2):359–371, 2010.

[28] X L. Li, D. Fu, and Y. Ma. Direct numerical simulation of hypersonic boundary layer transition over a blunt cone with a small angle of attack. *Physics of Fluids*, 22(2):025105, 2010.

[29] G. S. Jiang and C. W. Shu. Efficient implementation of weighted eno schemes. *Journal of Computational Physics*, 126(1):202–228, 1996.

[30] G. Dang, S. Liu, T. Guo, J. Duan, and X L. Li. Direct numerical simulation of compressible turbulence accelerated by graphics processing unit: An open-source high accuracy accelerated computational fluid dynamic software. *Physics of Fluids*, 34(12):126106, 2022.

[31] E. M. Gennaro, D. Rodríguez, M. A. F. Medeiros, and V. Theofilis. Sparse techniques in global flow instability with application to compressible leading-edge flow. *AIAA Journal*, 51(9):2295–2303, 2013.

[32] H B. E. Kurz and M J. Kloker. Receptivity of a swept-wing boundary layer to micron-sized discrete roughness elements. *Journal of Fluid Mechanics*, 755:62–82, 2014.

[33] H B. E. Kurz and M J. Kloker. Mechanisms of flow tripping by discrete roughness elements in a swept-wing boundary layer. *Journal of Fluid Mechanics*, 796:158–194, 2016.

[34] P. G. Huang, G. N. Coleman, and P. Bradshaw. Compressible turbulent channel flows: Dns results and modelling. *Journal of Fluid Mechanics*, 305:185–218, 1995.

[35] M. Bernardini, S. Pirozzoli, and P. Orlandi. Compressibility effects on roughness-induced boundary layer transition. *International Journal of Heat and Fluid Flow*, 35:45–51, 2012.

[36] M. Bernardini, S. Pirozzoli, P. Orlandi, and S K. Lele. Parameterization of boundary-layer transition induced by isolated roughness elements. *AIAA Journal*, 52(10):2261–2269, 2014.

[37] D Estruch-Samper, R .Hillier, L. Vanstone, and B. Ganapathisubramani. Effect of isolated roughness element height on high-speed laminar–turbulent transition. *Journal of Fluid Mechanics*, 818, 2017.

[38] T. Sayadi and P J. Schmid. Parallel data-driven decomposition algorithm for large-scale datasets: with application to transitional boundary layers. *Theoretical and Computational Fluid Dynamics*, 30(5):415–428, 2016.

[39] H. Choi and P. Moin. On the space-time characteristics of wall-pressure fluctuations. *Physics of Fluids*, 2(8):1450–1460, 1990.

[40] W. Heisenberg. Zur statistischen theorie der turbulenz. *Zeitschrift für Physik*, 124(7):628–657, 1948.

[41] Y S. Zhang, W T. Bi, F. Hussain, and Z S. She. A generalized reynolds analogy for compressible wall-bounded turbulent flows. *Journal of Fluid Mechanics*, 739:392–420, 2014.

[42] J. Jiménez, S. Hoyas, M P. Simens, and Y. Mizuno. Turbulent boundary layers and channels at moderate reynolds numbers. *Journal of Fluid Mechanics*, 657:335–360, 2010.

[43] M. Cogo, F. Salvadore, F. Picano, and M. Bernardini. Direct numerical simulation of supersonic and hypersonic turbulent boundary layers at moderate-high reynolds numbers and isothermal wall condition. *Journal of Fluid Mechanics*, 945:A30, 2022.